Spring 2020

Activation of Nitrite and Carbon Dioxide by Cobalt Centered Redox Active Ligand Featuring a Hemilabile Pendant Amine

Douglas F. Baumgardner
Western Washington University, douglasbaumgardner@gmail.com

Activation of Nitrite and Carbon Dioxide by Cobalt Centered Redox Active Ligand Featuring a Hemilabile Pendant Amine

By

Douglas F. Baumgardner

Accepted in Partial Completion
of the Requirements for the Degree
Master of Science

ADVISORY COMMITTEE

Dr. John D. Gilbertson, Chair

Dr. Margaret L. Scheuermann

Dr. David Rider

GRADUATE SCHOOL

David L. Patrick, Interim Dean

Master's Thesis

In presenting this thesis in partial fulfillment of the requirements for a master's degree at Western Washington University, I grant to Western Washington University the non-exclusive royalty-free right to archive, reproduce, distribute, and display the thesis in any and all forms, including electronic format, via any digital library mechanisms maintained by WWU.

I represent and warrant this is my original work, and does not infringe or violate any rights of others. I warrant that I have obtained written permissions from the owner of any third party copyrighted material included in these files.

I acknowledge that I retain ownership rights to the copyright of this work, including but not limited to the right to use all or part of this work in future works, such as articles or books.

Library users are granted permission for individual, research and non-commercial reproduction of this work for educational purposes only. Any further digital posting of this document requires specific permission from the author.

Any copying or publication of this thesis for commercial purposes, or for financial gain, is not allowed without my written permission.

Douglas F. Baumgardner

June 2020

Activation of Nitrite and Carbon Dioxide by Cobalt Centered Redox Active Ligand Featuring Hemilabile Pendant Amine.

A Thesis
Presented to
The Faculty of
Western Washington University

In Partial Fulfillment
Of the Requirements for the Degree
Master of Science

by
Douglas F. Baumgardner
June 2020

Abstract

Carbon dioxide (CO_2) and bioavailable nitrogen in the form of nitrates (NO_3^-) and nitrites (NO_2^-) are serious environmental pollutants. However, without economic incentives there is little interest in remediation of these pollutants outside of laboratory scale experiments. CO_2 can be converted to carbon monoxide (CO), a valuable building block in Fischer-Tropsch sourced fuel, and NO_3^- and NO_2^- can be converted to ammonia, another important chemical building block. However, both require effective, low-cost catalysts to be financially viable options. This thesis seeks to demonstrate the conversion of CO_2 to CO as well as NO_3^- and NO_2^- reduction. To accomplish this a cobalt centered redox active pyridine diimine ligand scaffold with an appended hemilabile, proton responsive pyridine ring (^{Pyrr}PDI) was synthesized. The ^{Pyrr}PDI scaffold is capable of storing multiple electron equivalents, making it ideal for small molecule activation where several electrons are often required. Reduction of the complex was carried out through chemical and electrochemical means. Once reduced this complex shows activity toward both CO_2 and NO_2^-, releasing CO and/or NO gas. When acid is introduced the complex showed electrocatalytic activity toward NO_2^-, with small amounts of ammonia being produced though the primary product of that reaction is currently unknown. An unexpected reaction between Samarium diiodide (SmI_2) being used as a chemical reductant and nitrite lead to examination of SmI_2 as a means to convert various nitrogen oxides to N_2.

Acknowledgments

Research Advisor:	Dr. John D. Gilbertson
Thesis Committee:	Dr. Margaret L. Scheuermann Dr. David Rider
Research Group Members:	Walker Marks, Matt Smiley, Wyatt Parks, Hanlei Lewine, Allison Teagan, April Trausch
Instrument Technicians:	Dr. Hla Win-Piazza, Sam Danforth, Charles Wandler, Sarina Kiesser, Kimberly Wurth
Mass Spectroscopy:	Dr. John Antos
X-ray Crystallographers:	Dr. Lev Zakharov, Dr. Orion Berryman, Dr. Eric Reinheimer, Daniel Decato
Financial Support:	National Science Foundation, Western Washington University Graduate School National Institutes of Health

Western Washington University Department of Chemistry

Table of Contents **page**

List of Tables and Figures

List of Abbreviations

Å	Angstrom
MeCN	Acetonitrile
Atm	Atmosphere
BE	Bulk electrolysis
CV	Cyclic Voltammogram
DCM	Dichloromethane
DNIC	Dinitrosyl Iron Complex
e^-	Electron
FT-IR	Fourier Transform Infrared
GC	Gas Chromatography
h	Hour
h^{-1}	Per Hour
MS	Mass spectrometry
NMR	Nuclear Magnetic Resonance
ORTEP	Oak Ridge Thermal Ellipsoid Plot
ppm	parts per million
H^+	Proton
PDI	Pyridinediimine
THF	Tetrahydrofuran
TOF	Turnover Frequency
TON	Turnover Number
UV-Vis	Ultraviolet-Visible
V	Volts

Chapter 1: Introduction

1.0 Small Molecule Activation

Small molecules, such as H_2, N_2, CO, CO_2, and ions, such as NO_3^- and NO_2^-, are ubiquitous through nature, and their abundance makes them enticing targets for chemical feedstocks.[1] However, many are relatively inert and require a catalyst for transformation into higher value reagents.[2,3] One prominent example is the Haber-Bosch process, wherein N_2 and H_2 are combined at high pressure and temperature over an iron/aluminum oxide catalyst to produce NH_3.[3] This process consumes roughly 1% of the total energy supply,[4] is a major contributor to CO_2 pollution,[3] and feeds roughly half the world's population. Nature, however, uses a metalloenzyme, nitrogenase, to perform this same reaction at room temperature and pressure.[5]

Remediation of environmental pollutants, like NO_2^- and CO_2 is an issue humanity needs to address. Aside from CO_2 emissions, the release of significant amounts of bioavailable Haber-Bosch sourced nitrogen in the forms of NO_3^- and NO_2^- is a major issue. This excess bioavailable nitrogen can lead to out of control growth of microorganisms in waterways, resulting in oxygen deprived dead zones.[6] The use of these pollutants as feedstocks is an appealing idea for the remediation of environmentally harmful compounds.

1.1 Metalloenzymes

Nature utilizes metalloenzymes to accomplish a wide array of otherwise difficult transformations, including nitrogen fixation and photosynthesis.[7] These metalloenzymes can serve as inspiration for human-made catalysts. For example *cd*$_1$ nitrite reductase facilitates the six electron transformation of NO_2^- to ammonia[5] (eq. 1), an important reaction for remediation of excess Haber-Bosch sourced nitrogen.

$$NO_2^- + 6e^- + 8H^+ \longrightarrow NH_4^+ + 2H_2O \qquad \textbf{(1.1)}$$

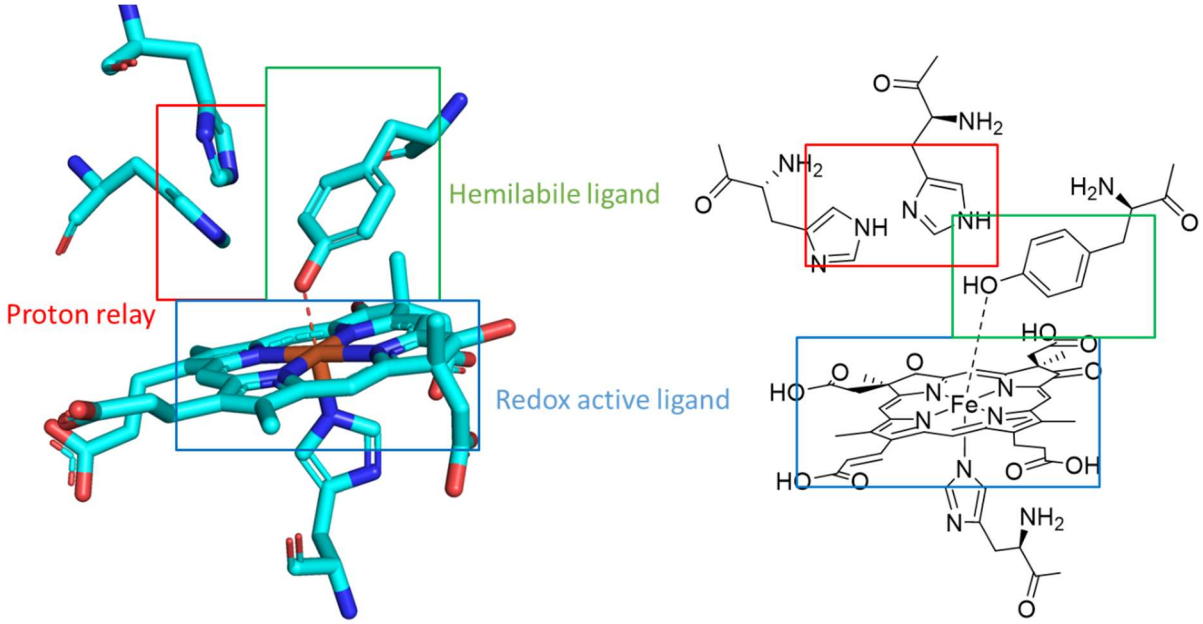

Figure 1.1 Nitrite Reductase Cytochrome *cd*$_1$ Left: Chemdraw and Right: PyMOL representation (PDB: 1HJ5). Hemilabile (green), proton responsive (red) and redox active (blue) motifs highlighted

This metalloenzyme (Fig 1.1) utilizes several important motifs to efficiently achieve the desired reactivity. It features two conserved histidine residues in the secondary coordination sphere that form an electropositive pocket to attract the negatively charged NO_2^- ion, and act as a proton relay. Additionally, it features a hemilabile tyrosine ligand which helps to stabilize resting states and a redox active heme ligand.

Galactose oxidase (Fig 1.2) is a well-studied enzyme which oxidizes primary alcohols to aldehydes, coupled with the reduction of dioxygen to hydrogen peroxide.[8,9] While this reactivity is not the focus of this thesis, the mechanisms utilized are.

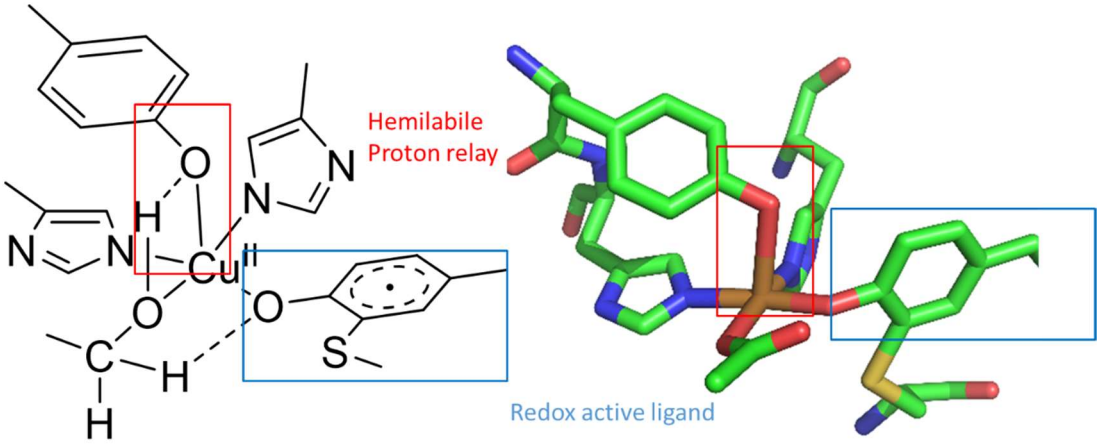

Figure 1.2 Galactose Oxidase Left: Chemdraw and Right: PyMOL representation (PDB: 1GOF) Hemilabile, proton responsive (red) and redox active (blue) motifs highlighted

Galactose oxidase features a proton-responsive (able to accept and donate a proton) and hemilabile (able to vary binding mode based on intramolecular changes) tyrosine residue,[9] which plays an active role in the catalytic cycle, rather than stabilizing a resting state as observed in nitrite reductase. Additionally, it has a redox active modified tyrosine which provides a ligand centered radical,[10–14] allowing for efficient shuttling of electrons in and out of the metal center.[12] The combination of these three motifs in around a metal center lead to the remarkably fast reactivity of galactose oxidase.[9]

1.2 Synthetic Models

Synthetic models of metalloenzymes seek to draw inspiration from nature to perform similar reactions, or to study the mechanism nature uses.[15] A prime example of the latter case is the bispyrrole-trispyridine, 2,2′,2′-methylbispyridyl-6-(2,2′,2′-methylbis-5-cyclohexyliminopyrrol)-pyridine ($Py_2Py(pi^{Cy})_2$)[16] system, recently published, which explored the mechanism of action of nonheme iron 2-oxogluterate enzymes (Fig 1.3).

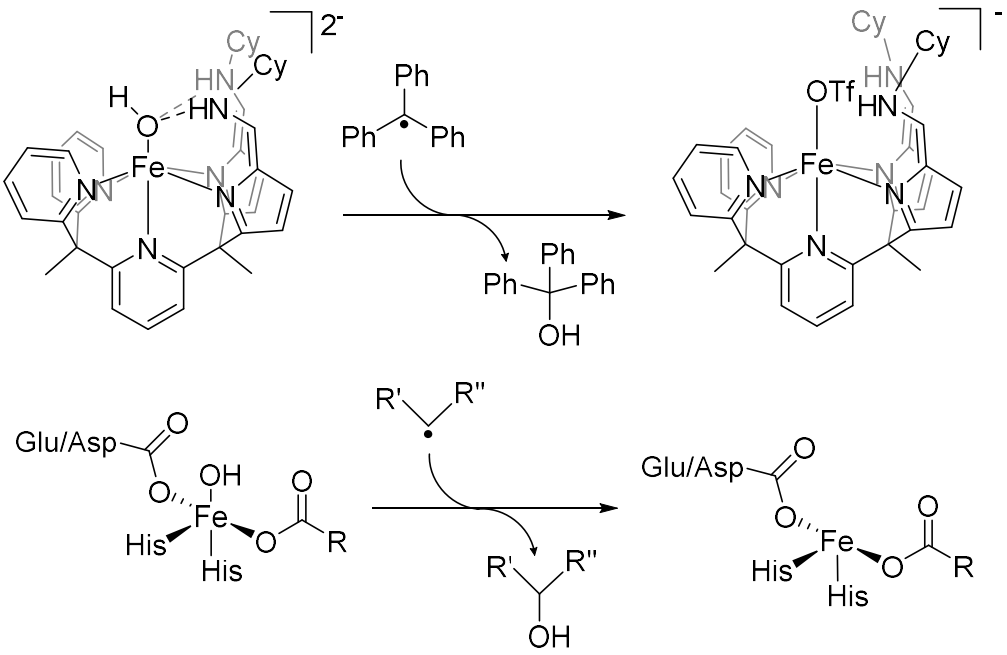

Figure 1.3 $Py_2Py(pi^{Cy})_2$ system and nonheme iron 2-oxogluterate reaction.[16]

The $Py_2Py(pi^{Cy})_2$ system was characterized at each step as the compound was reacted through the stepwise addition of electrons and protons. To test the radical rebound hypothesis[17] of nonheme iron 2-oxogluterate, where the iron-bound oxygen species is abstracted by and organic radical, a similar reaction to that of the enzyme was performed.

Drawing inspiration from nitrate reductase for similar reactivity is the (tris(5-cycloiminopyrrol-2-ylmethyl)amine ($H_3[N(pi^{Cy})_3]$)[18] system was able to catalytically reduce NO_3^- to nitric oxide (NO) using a sacrificial reductant (Fig 1.4). By tuning the secondary coordination sphere to orient the target molecule a preferred binding mode can be promoted, leading to increased activity.

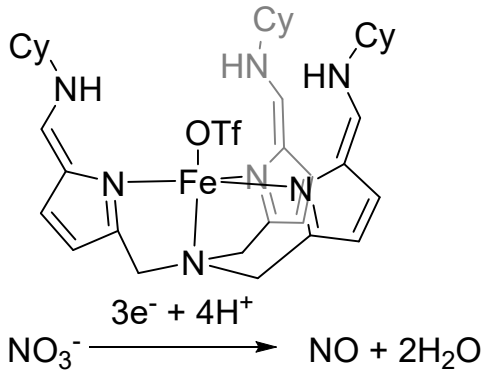

Figure 1.4 Bioinspired ($H_3[N(pi^{Cy})_3]$) system for catalytic reduction of NO_3^-.[18]

1.3 Hemilability

As noted previously, Nature uses hemilability, or the reversible binding of a ligand to a metal center, to stabilize high energy intermediates or as an active part of catalytic cycles.[19] The term hemilability was popularized in 1979[20] in reference to the variable binding of phosphine-ether ligands binding to a ruthenium metal center (Fig 1.5).

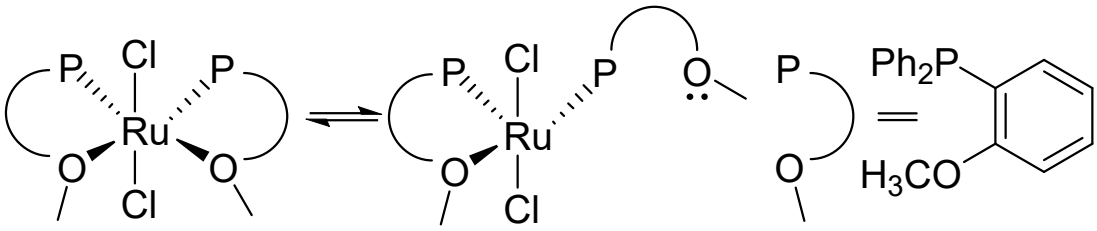

Figure 1.5 Hemilability demonstrated with a phosphine-ether system.[20]
P-O = o-(diphenylphosphino)anisole.

The result of this variable binding motif is that there is an open coordination site in equilibrium with the weakly bound ligand.[21] As most metal-based chemistry requires at least one open coordination site this can be exploited to greatly increase the activity of metal containing compounds.[19,21–26]

1.4 Redox-Active Ligands

The transformation of most small molecules requires the movement of multiple electrons, but low-cost earth abundant first row transition metals typically transfer single electron equivalents.[27] A potential way around this problem is to use a redox-active ligand. In these systems, electron equivalents are stored in pi systems as ligand centered radicals. The pyridinediimine (PDI) ligand scaffold is capable of holding two electron equivalents which makes it a valuable tool[28–30] for reactions requiring two or more electrons.

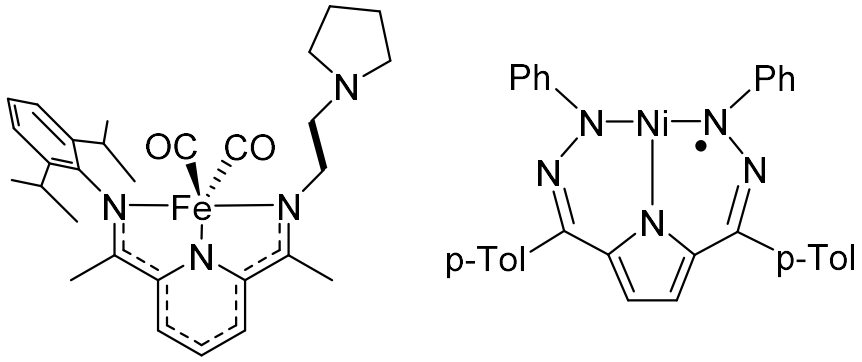

Figure 1.6 Ligand centered radicals in redox non-innocent ligands represented as dispersed through the pi system in the ^{Pyrr}PDI (left) or localized to a specific heteroatom in the dihydrazonopyrrole 2,5-bis((2-phenylhydrazono)(p-tolyl)methyl)-pyrrole system (right).

1.5 Objectives

The research presented herein will primarily focus on the activity of $Co^{Pyrr}PDI(OTf)_2$ (Fig 1.7) with NO_2^-. This work draws from previous work in this lab using $Fe^{Pyrr}PDI$ for the reduction of NO_2^- (Scheme 1.1). In the case of $Fe^{Pyrr}PDI$ the reduction of NO_2^- leads to a dinitrosyl iron complex (DNIC) which, due to very stable electronics,[31] is essentially inert.

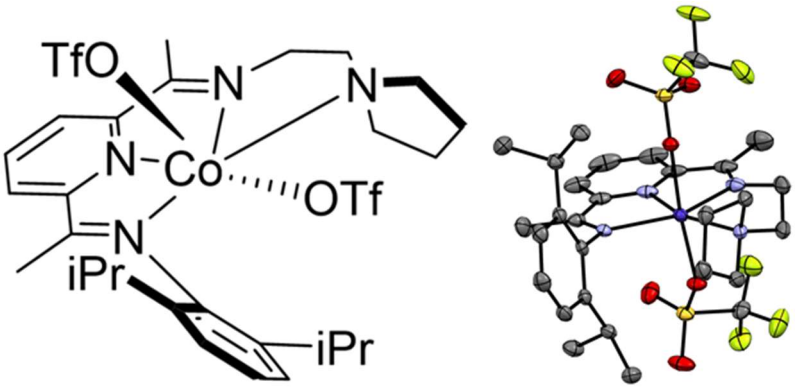

Figure 1.7 ORTEP representation of crystal structure of $Co^{Pyrr}PDI(OTf)_2$ (right), H atoms omitted for clarity, and Chemdraw of $Co^{Pyrr}PDI(OTf)_2$ (left).

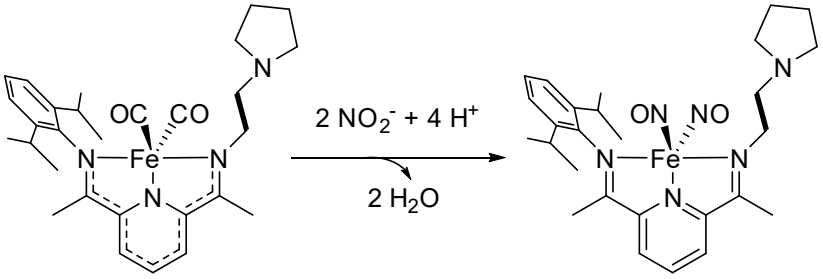

Scheme 1.1. Reduction of NO_2^- by $Fe^{Pyrr}PDI(CO)_2$ and formation of DNIC $Fe^{Pyrr}PDI(NO)_2$

It is hypothesized that the use of cobalt in place of iron will shift the electronics sufficiently to cause the nitrosyl groups to become labile, potentially allowing for catalytic reduction of NO_2^- with a sacrificial reductant. Electrochemical reduction is also explored in this thesis in place of a sacrificial chemical reductant. There is precedent[32] for the catalytic reduction of NO_2^- to ammonia using a four coordinate cobalt centered ligand, and this will be tested for in electrochemical experiments (Fig. 1.8).

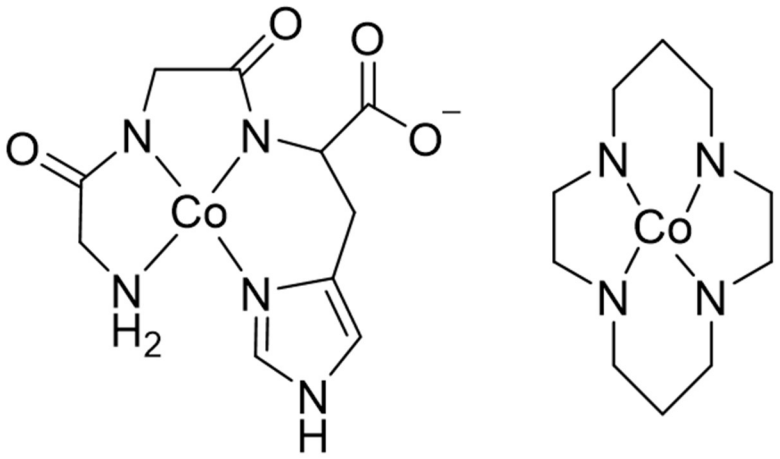

Figure 1.8 GlyGlyHis Metallopeptide (left) and cobalt cyclam (right) that show electrocatalytic activity towards NO_2^-.

The cobalt cyclam[33] has multiple electrocatalytic products, with hydroxylamine (NH_2OH) and NH_4^+ as products with turnover frequencies (TOF) of 433 hr^{-1} and 229 hr^{-1} and turnover numbers (TON) of 494 and 332 respectively. However the metallopeptide[32] shows complete selectivity for NH_4^+ with a TOF of 813 hr^{-1} and a TON of 3250. The metrics TON refers to the number of times a catalyst can complete a catalytic cycle on average before becoming poisoned and TOF refers to the frequency with which it completes a catalytic cycle.

The reduction of CO_2 to CO has also previously been shown using iron centered PDI scaffolds,[34] and will be explored in this thesis using a hemilabile pendant amine and cobalt center, with the hypothesis that the shift in electronics coupled with the stabilizing effect of the hemilabile arm may show catalytic turnover.

In a secondary project the reactivity of samarium diiodide (SmI_2) with N_2O is explored. While there are reports of using Sm (II) with bulky ligands to form bridging oxo compounds[35] by reduction of N_2O, the gaseous products are not tracked. Here, using SmI_2 the gaseous product of the reduction of N_2O is reported as N_2, in quantitative yield.

Chapter 2: Synthesis of Co^{Pyrr}PDI compounds

2.0 – Synthesis of Co^{Pyrr}PDI(OTf)$_2$

As mentioned in Chapter 1, the Fe^{Pyrr}PDI system has previously been published[36] showing the ability to reduce NO_2^- to mono- and dinitrosyl iron complexes.

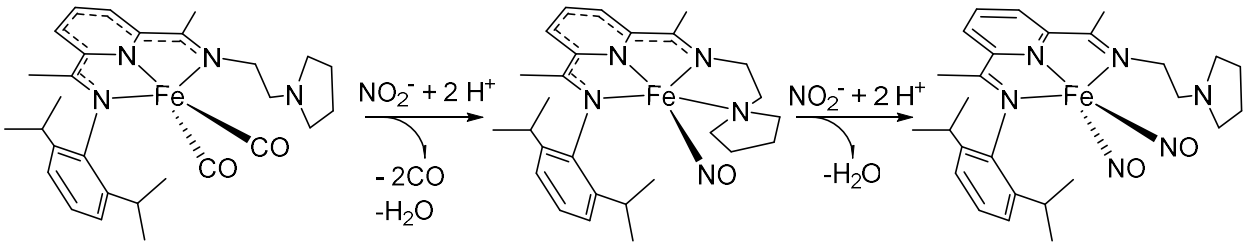

Scheme 2.1 Fe^{Pyrr}PDI reduction of NO_2^- to mono- and dinitrosyl iron complexes

Due to the unusual electronic structure of DNICs[31] (their electrons are shared between the iron center and the redox non-innocent nitrosyl ligands) the nitrosyl ligands tend to be inert. By shifting from d^8 iron to d^9 cobalt the electronics of the system may be shifted while remaining in the arena of relatively inexpensive first row transition metals.

Synthesis of the ^{Pyrr}PDI system followed previously published work,[36] starting with 2,6-diacetylpyridine and performing sequential Schiff-base condensations with 2,6-diisopropylaniline and 1-(2-aminoethyl)pyrrolidine.

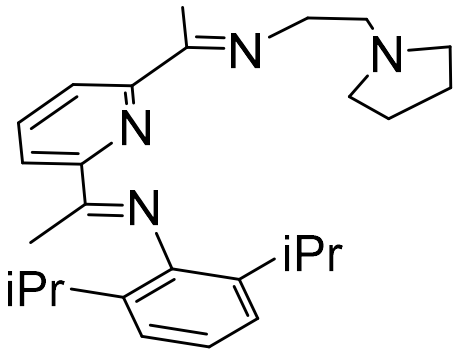

Figure 2.1 Chemdraw representation of the ^{Pyrr}PDI ligand

To metallate the ^{Pyrr}PDI ligand, the ligand and one equivalent of $Co(OTf)_2$ are added to a 20 mL scintillation vial charged with a magnetic stir bar and about 5 mL MeCN (eq. 2.1). As neither the ligand nor metal source are very soluble in MeCN, the result is a slurry. After stirring overnight, the reaction yields a deep red solution which is filtered through celite and solvent is removed by evaporation under reduced pressure. Redissolving the solid in MeCN and layering with diethyl ether or layering with diethyl ether directly results in red crystals of $Co^{Pyrr}PDI(OTf)_2$ in 80% yield.

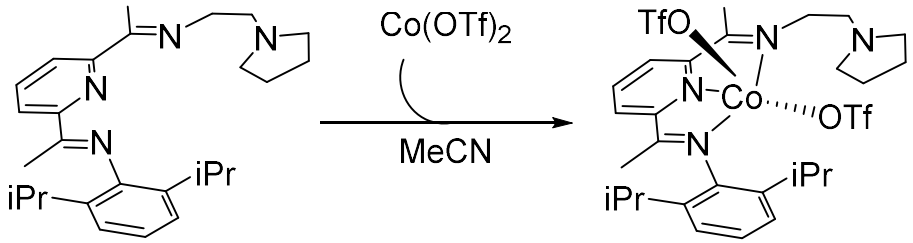

(**2.1**)

2.1 – Electrochemical studies of $Co^{Pyrr}PDI(OTf)_2$

As the target for this work was the remediation of environmental contaminants to less harmful, or value-added products, understanding the ability of the $Co^{Pyrr}PDI(OTf)_2$ system to accept and move electrons is very important. As shown in eq. 1.1 the transformation of nitrite to ammonium requires six electrons, making this process difficult for many synthetic systems. However, in the case of an electrocatalyst the electrons are supplied by a potentiostat, mitigating the need for a system to store several equivalents of electrons.

To better understand if $Co^{Pyrr}PDI(OTf)_2$ can act as an electrocatalyst characterization of the electronics were carried out using cyclic voltammetry (Fig 2.2). In these studies, two reversible events were identified (E ½ = -0.7 V vs Fc, E ½ = -1.7 V vs Fc) indicating that $Co^{Pyrr}PDI(OTf)_2$ can be reduced twice without significant change to the system. To further test these results

chemical reduction of $Co^{Pyrr}PDI(OTf)_2$ was performed by passing a solution of it through a KC_8 plug and analyzing the resultant solution by the same methods. This resulted in a shift of the open circuit potential (OCP), or resting electronic state of the analyte,[37] of -0.4 V, to the other side of the first reversible event with no significant change to the character of the cyclic voltammogram (CV). This result indicated that the $Co^{Pyrr}PDI(OTf)_2$ system is capable of storing an electron without significantly altering the molecule.

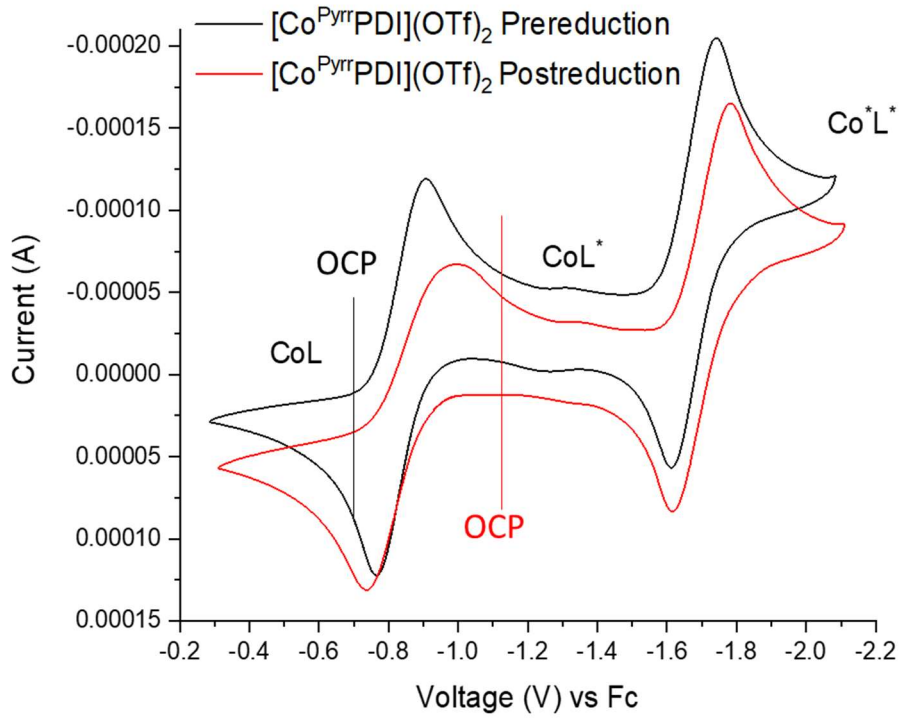

Figure 2.2. CV of 5 mM $Co^{Pyrr}PDI(OTf)_2$ before and after chemical reduction by method 1 in MeCN WE: Glassy carbon, RE: $Ag/AgNO_3$ CE: Pt wire 0.2 M $TBAPF_6$ electrolyte. OCP Prereduction: -0.7 V Post reduction -1.1 V vs Fc

To examine the potential for electrocatalysis in this system several controls were performed (Fig 2.3). In these controls the acid source, trifluoroethanol (TFE), is tested alone, with the nitrite source, tetrabutylammonium nitrite ($TBANO_2$), and $Co^{Pyrr}PDICl_2$. Once the

controls were completed $Co^{Pyrr}PDICl_2$ was tested with TFE and $TBANO_2$, where it showed a catalytic current well positive of any other observed events. While this does not identify products, it provides proof that the system is electrocatalytically active when nitrite and acid are present.

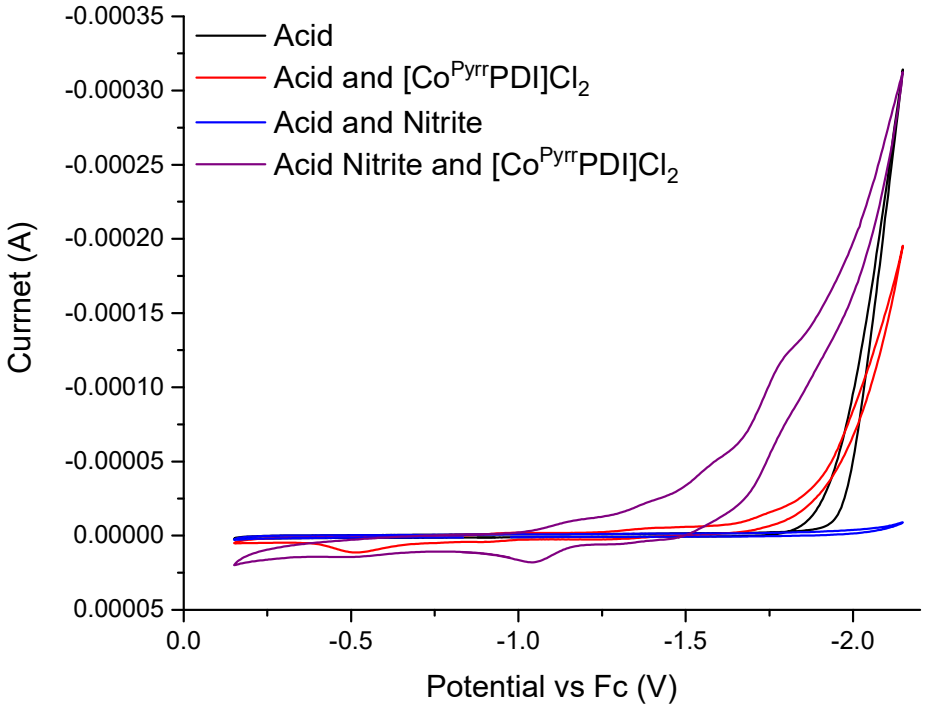

Figure 2.3. CV of TFE (black); TFE and $TBANO_2$ (blue); TFE and $Co^{Pyrr}PDICl_2$ (red); TFE, $TBANO_2$ and $Co^{Pyrr}PDICl_2$ (purple)

As the compound of interest is $Co^{Pyrr}PDI(OTf)_2$ it was then compared in the same conditions as $Co^{Pyrr}PDICl_2$ where it showed a similar catalytic profile (Fig 2.4).

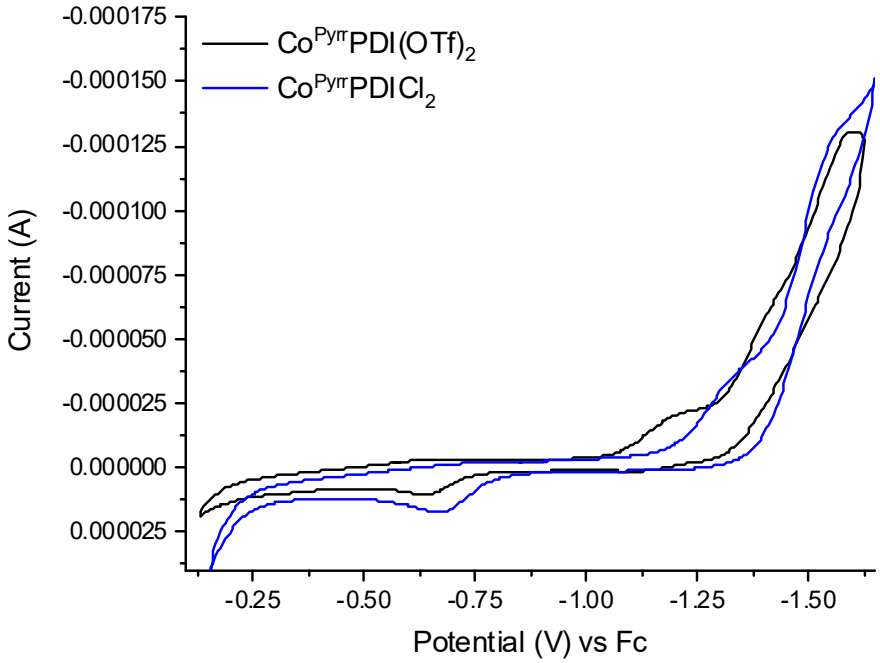

Figure 2.4. CV of $Co^{Pyrr}PDI(OTf)_2$ (blue) and $Co^{Pyrr}PDICl_2$ (black)

With the characterization of the electronics of the $Co^{Pyrr}PDI(OTf)_2$ system, as well identification of potential electrocatalytic conditions bulk electrolysis (BE) experiments can be conducted. In BE experiments a potential is held for a time while current is passed, allowing for the flow of electrons. The constant flow of electrons allows for continuous catalytic transformation of substrate (NO_2^-) to product (NH_4^+)

2.2 – Synthesis of [$CoH^{Pyrr}PDI(CO)I$][I]

To isolate intermediates for the elucidation of reaction mechanisms as well as characterization of reduced intermediates, chemical reduction is a useful tool even for electrocatalysts. Reduced species can, however, be difficult to isolate. One tool for stabilizing

reduced chemical species is to tune the ligand field, such as with carbon monoxide (CO).[38] For this reason chemical reduction was performed under a CO atmosphere.

In a Fischer-Porter tube $Co^{Pyrr}PDI(OTf)_2$ was mixed with one mole equivalent of SmI_2 in THF. The tube was then sealed and removed from the box, then charged with 30 psi CO as in equation 2.2.

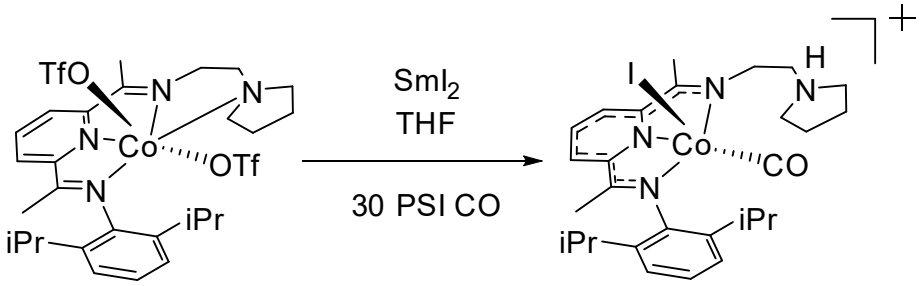

(2.2)

The reaction mixture was allowed to stir overnight, and the solvent was removed under reduced pressure. Washing the solid with diethyl ether resulted in a red solution, which upon evaporation yielded long red crystals which were not of X-ray quality. Dissolving the remaining solid in MeCN yielded a green solution, and when layered with diethyl ether yielded green crystals of X-ray quality (42% yield).

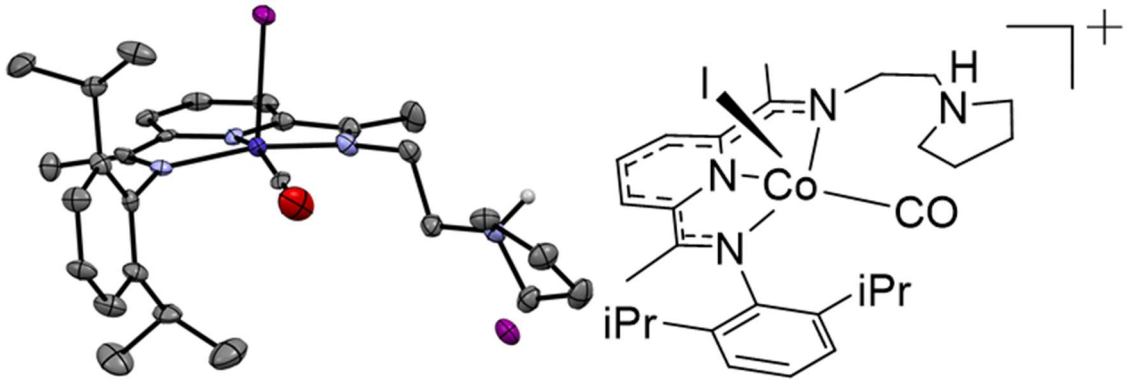

Figure 2.5. ORTEP representation of crystal structure of $[CoH^{Pyrr}PDI(CO)I][I]$ (left), H atoms omitted for clarity, and Chemdraw of $[CoH^{Pyrr}PDI(CO)I][I]$ (right).

The compound crystalized with the pyrrolidine arm protonated, though no source of protons was added to the mixture. Later analysis of the headspace of the Sure/Seal™ bottle of SmI_2 used revealed H_2 in the headspace. The most likely source of this H_2 is adventitious water in the THF used by commercial sources. Since there is an I^- counterion to the molecule this seems the most likely source of the proton, as there would be an abundance of I^- available in the SmI_2 solution but not later, such as if the proton was abstracted from adventitious water in MeCN during crystallization.

Analysis of the bonds in the reduced vs. non-reduced $Co^{Pyrr}PDI$ indicates that the ligand accepts the electron and becomes reduced, rather than the metal center (Fig 2.6).

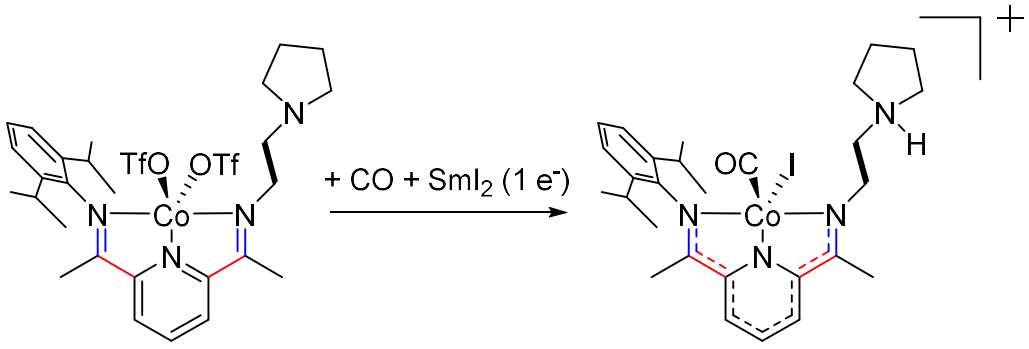

Figure 2.6. Reduction of $Co^{Pyrr}PDI(OTf)_2$ to $[CoH^{Pyrr}PDI(CO)I][I]$ with N_{imine}-C_{imine} bonds highlighted in blue and C_{imine}-C_{ipso} bonds highlighted in red.

The N_{imine}-C_{imine} bonds elongate (1.289 Å, 1.268 Å to 1.317 Å, 1.311 Å) and the C_{imine}-C_{ipso} bonds contract (1.493 Å, 1.493 Å to 1.441 Å, 1.446 Å). This is due to the N_{imine}-C_{imine} bonds losing some double bond character and the C_{imine}-C_{ipso} bonds gaining some double bond character. The delocalization of an electron along the conjugated backbone is responsible for these changes, suggesting that the metal center is still Co (II).

The $Co^{Pyrr}PDI(OTf)_2$ system was synthesized and characterized via CV and X-ray crystallography. Identification of possible catalytic conditions were carried out, also using CV. The singly reduced species $[CoH^{Pyrr}PDI(CO)I][I]$ was synthesized and characterized via X-ray crystallography. Bond length analysis was used to identify where the electron resides. Using this information chemical and electrochemical reduction of small molecules will be performed.

Chapter 3: Small molecule activation using $Co^{Pyrr}PDI(OTf)_2$

3.0 – Electrochemical NO_2^- Reduction

As stated above, The six electron eight proton transformation of nitrite to ammonium (eq. 1.1) can be difficult for synthetic systems.[5] While several electrocatalysts for this transformation have been reported, they often require high potential,[39] or suffer from poor selectivity.[40] An example of an electrocatalyst that is highly selective for ammonium, operates at relatively mild potential (-0.66 V vs. SHE) and has a high turnover rate is the four coordinate cobalt metallopeptide (Fig).[32] Like $Co^{Pyrr}PDI(OTf)_2$ it features Co(II) nestled in a nitrogen pocket with a proton responsive ligand.

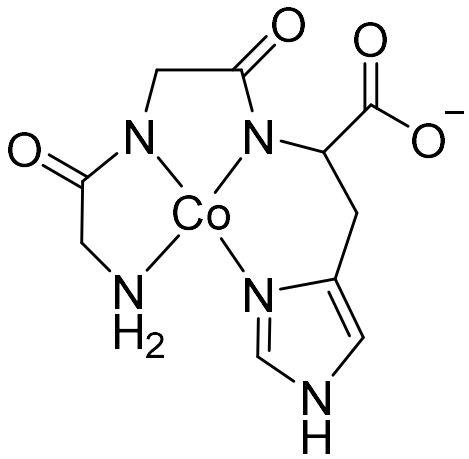

Figure 3.1. Chemdraw of cobalt metallopeptide[32] that shows selective electrocatalytic activity for the reduction of nitrite to ammonium.

In order to examine the electrochemical properties of $Co^{Pyrr}PDI(OTf)_2$ controls were carried out in chapter 2.1. While these controls showed the potential of electrocatalytic activity in order to test the efficacy of $Co^{Pyrr}PDI(OTf)_2$ as an electrocatalyst BE must be performed. In BE a constant potential is held and the current is measured over time. The area under this curve is equal to total charge passed, in Coulombs (C). This value can then be converted to electrons passed.

$$1\ \mathrm{C} = 6.424 \times 10^{18}\ e^- \qquad (\mathbf{3.1})$$

If products of the catalysis can be identified this can be used to determine a Faradaic efficiency of the catalyst, or for each electron put into the system how many are used to drive the reaction.

A sealed H-cell was charged with $Co^{Pyrr}PDI(OTf)_2$, tetrabutylammonium nitrite ($TBANO_2$), and trifluoroethanol (TFE) (as a proton source) in 30 mL of 0.1 M tetrabutylammonium hexafluorophosphate ($TBAPF_6$) electrolyte solution in MeCN. The potential was held at -1.5 V vs. Fc for 16 hours. During this time 16 C of charge (0.169 moles of electrons) was passed (Fig 3.2)

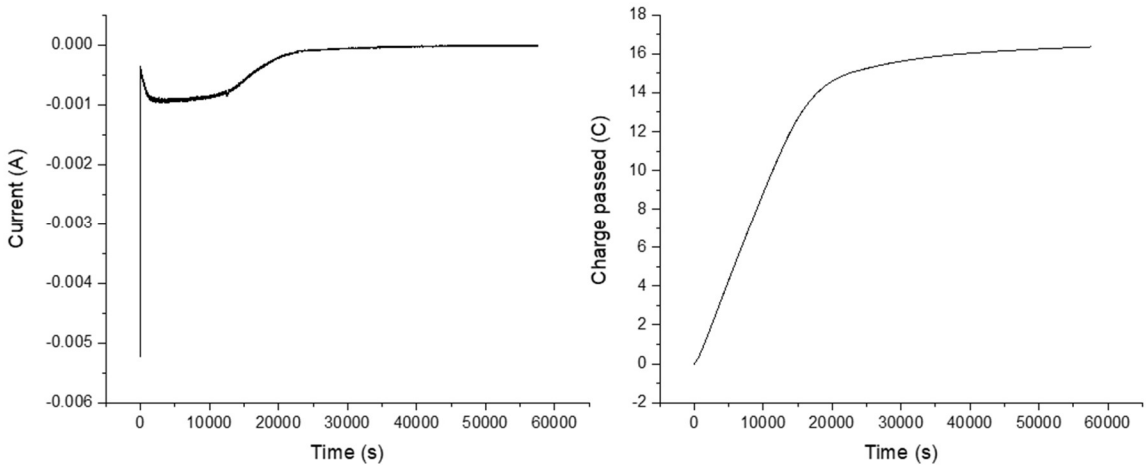

Figure 3.2. Bulk electrolysis of NO_2^- with six equivalents of TFE (relative to NO_2^-) as a miscible proton source and catalytic $Co^{Pyrr}PDI(OTf)_2$ in 0.1 M $TBAPF_6$ solution in MeCN held at -1.5 V vs. Fc for 16 hours (left) Current vs. time (right) charge passed vs. time from integration of current vs. time.

Analysis of the reaction headspace via FT-IR indicates that no IR active gases are evolved. Starting from NO_2^- this would rule out NO_2, N_2O, and NO. Other possible products from the reaction are hydroxylamine (NH_2OH), ammonium (NH_4) and N_2.

According to equations 3.3 and 3.4 respectively it requires two electrons and five protons to take NO_2^- to NH_2OH and a further two electrons and three protons to proceed to NH_4.

$$NO_2^- + 2e^- + 5H^+ \rightarrow NH_2OH + H_2O \quad (\mathbf{3.2})$$

$$NH_2OH + 2e^- + 3H^+ \rightarrow NH_4^+ + H_2O \quad (\mathbf{3.3})$$

Colorimetric testing for ammonium[41] showed a minimal response above baseline, indicating that this is not likely the primary product for the reaction. While colorimetric testing for hydroxylamine was inconclusive it remains a possible product of electrocatalysis using $Co^{Pyrr}PDI(OTf)_2$. Testing for N_2 as a product was not carried out, as the reaction was done under a N_2 atmosphere.

3.1 – Chemical NO_2^- Reduction

To attempt to definitively identify the products of the electrocatalytic reduction of NO_2^- chemical reduction was employed. By allowing for stepwise reactivity, and tighter control of electron and proton flux this technique affords more easily identified intermediates and products. The first step in this process was to react the reduced species [$CoH^{Pyrr}PDI(CO)I$][I] with $TBANO_2$.

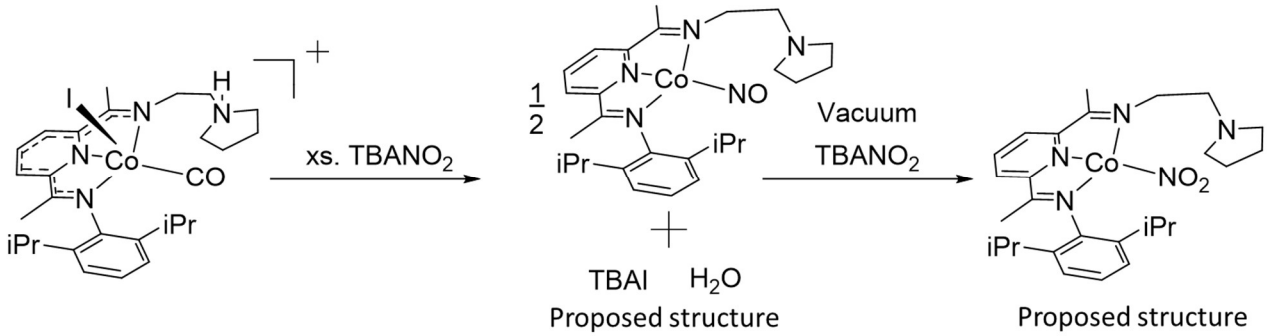

Scheme 3.1. Proposed reaction of [$CoH^{Pyrr}PDI(CO)I$][I] with NO_2^-.

A 25 mL sidearm reaction tube was charged with a magnetic stir bar, $TBANO_2$, and one equivalent of [$CoH^{Pyrr}PDI(CO)I$][I]. To this tube 10 mL of MeCN was added, the tube was sealed and stirring was turned on. The reaction was allowed to proceed overnight, after which time the headspace was sampled via gas phase IR. Following headspace sampling liquid cell IR measurements were gathered, and finally solid-state IR spectra were taken. By using isotopically labeled NO_2^- it is possible to track which signals in the IR are due to nitrogen sourced from said NO_2^- when comparing to an unlabeled IR spectrum. In the case of this reaction several signals are seen which can be linked to nitrogen sourced from reacted NO_2^-.

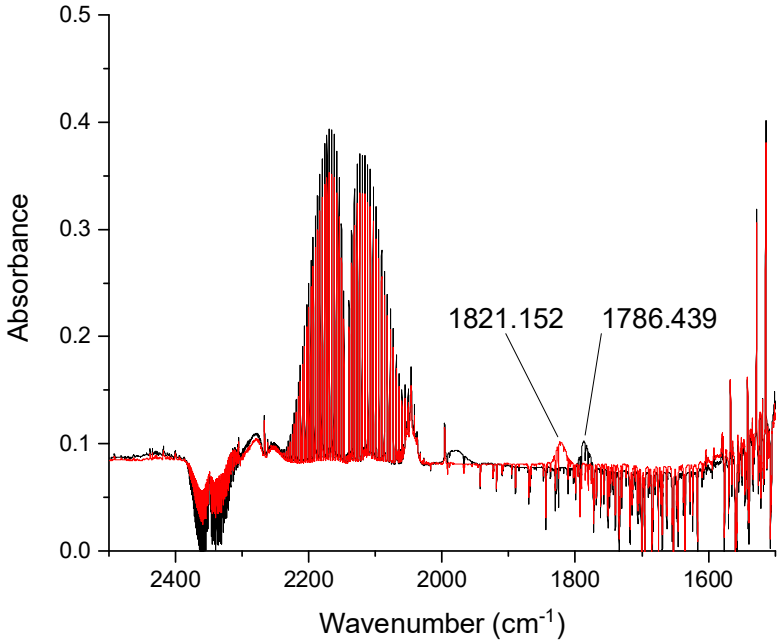

Figure 3.3. Gas phase FT-IR spectra of ^{14}N (red) and ^{15}N (black) labeled NO_2^- reduction using [CoH^{Pyrr}PDI(CO)I][I]. Labeled peals shift as expected from isotopic labeling.

The gas phase IR spectrum (Fig 3.3) shows no sign of nitrous oxide (N_2O) (centered at 2223 cm^{-1}), nitrogen dioxide (centered at 1630 cm^{-1}), or NO (centered at 1876 cm^{-1}). The release of the bound CO (2143 cm^{-1}) is a good indicator that a reaction is taking place, as the CO is likely being displaced for a different substrate. There is a nitrogen associated peak in the gas spectrum at 1821 cm^{-1} that shifts to 1786 cm^{-1} which is unassigned at this time.

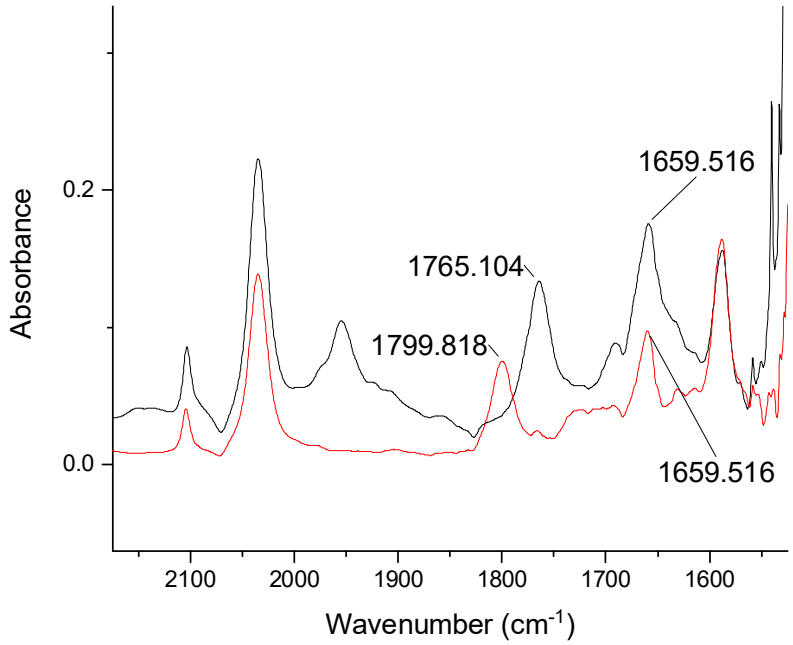

Figure 3.4. Liquid phase FT-IR spectra of ^{14}N (red) and ^{15}N (black) labeled NO_2^- reduction using [CoH^{Pyrr}PDI(CO)I][I]. Labeled peals shift as expected from isotopic labeling.

In the liquid cell IR spectrum (Fig 3.4), there is one peak which shifts with isotopic labelling, 1799 cm^{-1} to 1765 cm^{-1}, which is being assigned as a Co-NO stretch.

In the solid FT-IR spectrum there are several peaks which show shifts with isotopic labelling. These are assigned as bound NO_2^- (Fig 3.5).

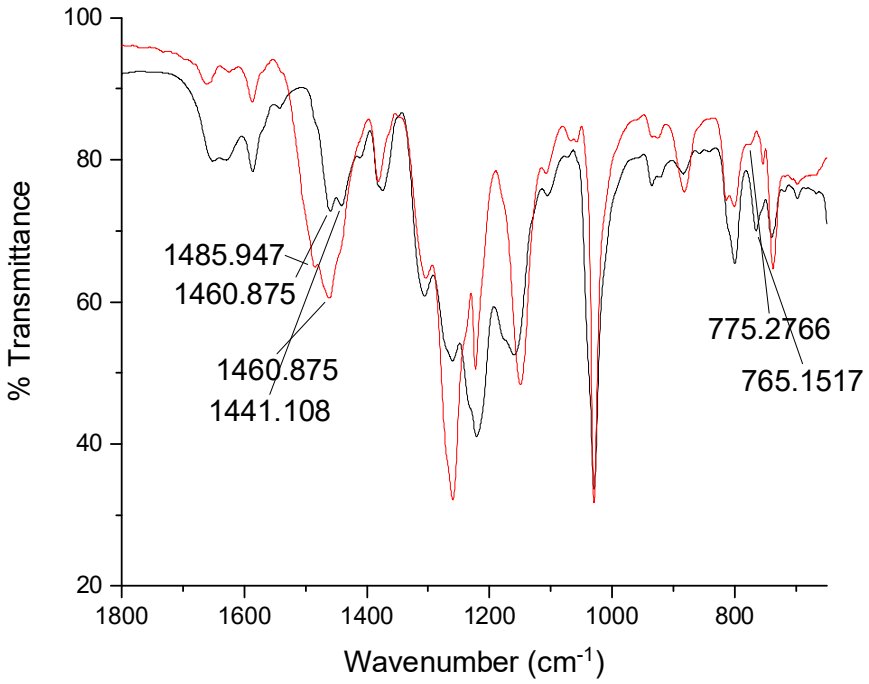

Figure 3.5. Solid phase AT-IR spectra of ^{14}N (red) and ^{15}N (black) labeled NO_2^- reduction using [CoH^{Pyrr}PDI(CO)I][I]. Labeled peals shift as expected from isotopic labeling.

In the chemical reduction of NO_2^- by [CoH^{Pyrr}PDI(CO)I][I] gaseous CO is observed, likely indicative of the PDI backbone losing the electron stored therein, which is evidence for a reaction occurring. In the liquid phase IR a peak was identified as a loosely bound NO, an intermediate in denitrification. In the condensed phase IR several peaks are due to nitrogen sourced from NO_2^- as verified by isotopic labeling and are attributed to bound NO_2^-. This is likely due a non-ideal stoichiometry being used; [CoH^{Pyrr}PDI(CO)I][I] provides one electron and one proton, but to eliminate an oxygen from NO_2^- as water two protons would be required.

3.2 – CO_2 reduction

An iron centered PDI compound has been previously been published showing catalytic reduction of CO_2 to CO.[34] However, after the reduction of CO_2 to CO the ligand is still in a reduced

state, and the CO are not labile, resulting in the need to oxidize the system with a strong acid to release the CO before re-reducing to begin the cycle again.

Additionally, a cobalt centered PDI compound was demonstrated to form CO bonds that could be interchanged with N_2 by varying the pressure of one gas vs. another.[42] By drawing inspiration from these two sources it was posited that using $Co^{Pyrr}PDI(OTf)_2$ CO_2 could be reduced to CO, then release the CO complex to a higher pressure of N_2.

A 25 mL sidearm reaction tube was charged with $Co^{Pyrr}PDI(OTf)_2$ and a magnetic stir bar and the sidearm was sealed with a septum. To this tube was then added one equivalent of 0.1 M SmI_2 in THF and the tube was removed from the glovebox. One equivalent of CO_2 was then introduced via gastight syringe. The reaction was then sealed and allowed to proceed overnight. The reaction mixture was then analyzed via gas and liquid phase FT-IR spectroscopy.

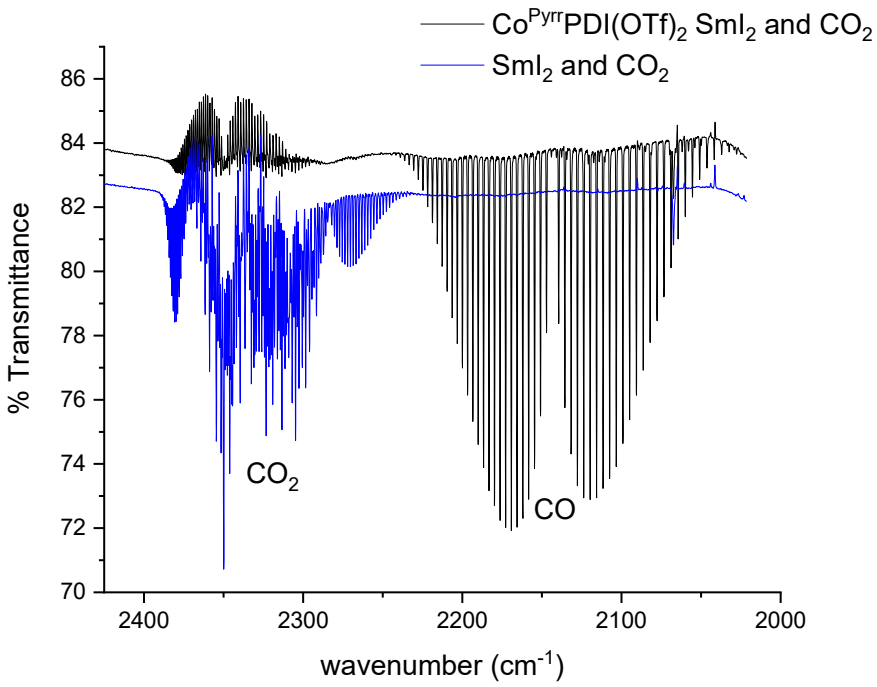

Figure 3.6. Gas phase FT-IR spectra of the headspace of a reaction of $Co^{Pyrr}PDI(OTf)_2$ with one equivalent of CO_2 and SmI_2 each (black) and CO_2 with one equivalent of SmI_2 as a control (blue).

The absorbance centered at 2143 cm^{-1} can be attributed to CO, resulting from the reduction of CO_2, and the lack of absorbance at 2349 cm^{-1} indicates that the full equivalent of CO_2 was consumed.

In the liquid cell experiment there was only one peak of interest, at 1961 cm^{-1}, which is near reported values published for Co-CO bands.[42] The nearness of this peak free CO (2143 cm^{-1}) indicates that there is not much π back-bonding occurring, which would weaken the C-O bond and shift it to lower wavenumbers. Additionally, as this CO peak is 78 wavenumbers higher than the CO peak of [CoH^{Pyrr}PDI(CO)I][I] it can be inferred that the system is less electron rich, and therefore not in the reduced state.

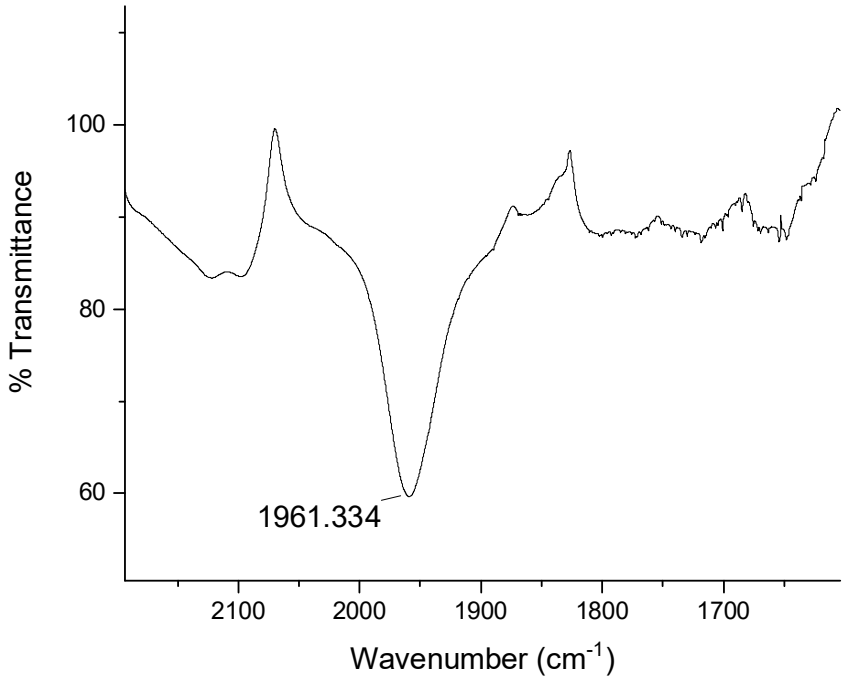

Figure 3.7. Liquid phase FT-IR spectra of a reaction of $Co^{Pyrr}PDI(OTf)_2$ with one equivalent of CO_2 and SmI_2 each showing Co-CO peak.

Chapter 4 – Reduction of N_2O by SmI_2

4.0 – N_2O Reduction

Nitrous oxide is potent greenhouse gas, 180 times more potent than CO_2.[43] The primary anthropogenic source of N_2O is agriculture, accounting for 85% of emissions in 2000.[44] Studies looking at the direct reduction of N_2O generally use very harsh conditions, high temperatures, or both and often still have poor yields.[45–47] Herein is discussed a method for the chemical reduction of N_2O to N_2 using a single reducing agent with good yields.

SmI_2, also known as Kagan's reagent, is a common catalyst in organic reactions, used in a wide range of organic reactions.[48,49] The use of SmI_2 as a nitro coupling reagent[50,51] was of particular interest to this work as a proposed mechanism features the elimination of oxygen from a N=N-O unit,[51] reminiscent of N_2O.

During the course of chemical NO_2^- reductions previously discussed in chapter 3 it was discovered that SmI_2 will react with NO_2^- to form N_2O (Fig 4.1).

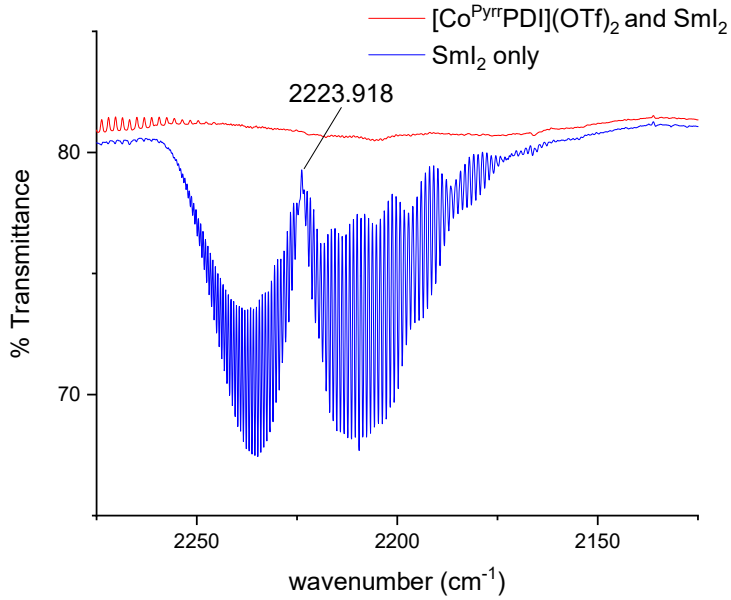

Figure 4.1. Control showing equal amounts of NO_2^- with SmI_2, with (red) or without (blue). Peak centered at 2223 cm^{-1} is N_2O.

There is literature precedent for bis(pentamethylcyclopentadienyl)samarium(II) (Cp^*_2Sm) reacting with NO and N_2O to form bridging oxo species,[35] however the gaseous products were not identified from the process. To begin a study of nitrogen oxides reactions with SmI_2 it was decided to begin closest to N_2, N_2O, and work on from there through NO, NO_2^- and NO_3^-. In this work, however, only the reaction with N_2O is examined.

In a typical experiment using a 25 mL sidearm reaction tube charged with a magnetic stir bar a 0.1 M solution of SmI_2 in THF is added, and the tube is sealed. This is followed by three rounds of freeze-pump-thaw to ensure the solution is thoroughly degassed. Finally, one or two equivalents of N_2O is added via gas tight syringe. The reaction mixture is allowed to stir for two days, at which point the solution will have gone from deep blue to yellow and a yellow precipitate will have formed.

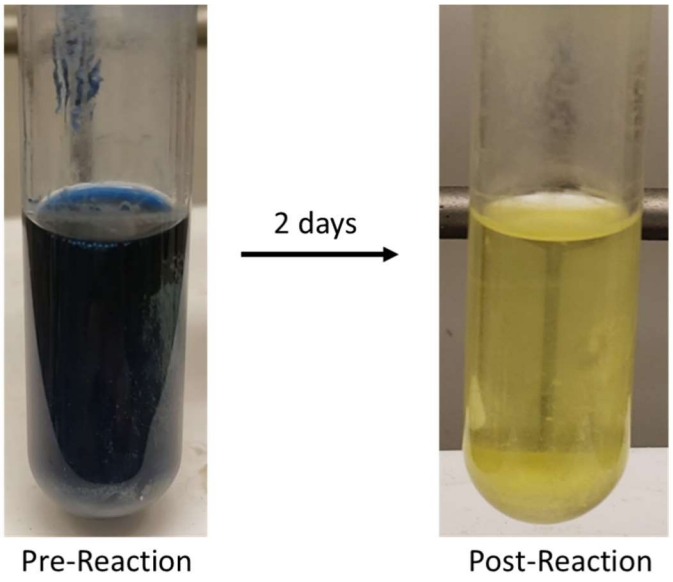

Figure 4.2. Samarium solutions in 25 mL reaction tubes before (left) and after (right) two-day reaction with N_2O.

Analysis of the headspace these reactions via gas chromatography (GC) shows production of N_2 and decreasing amounts of nitrous oxide.

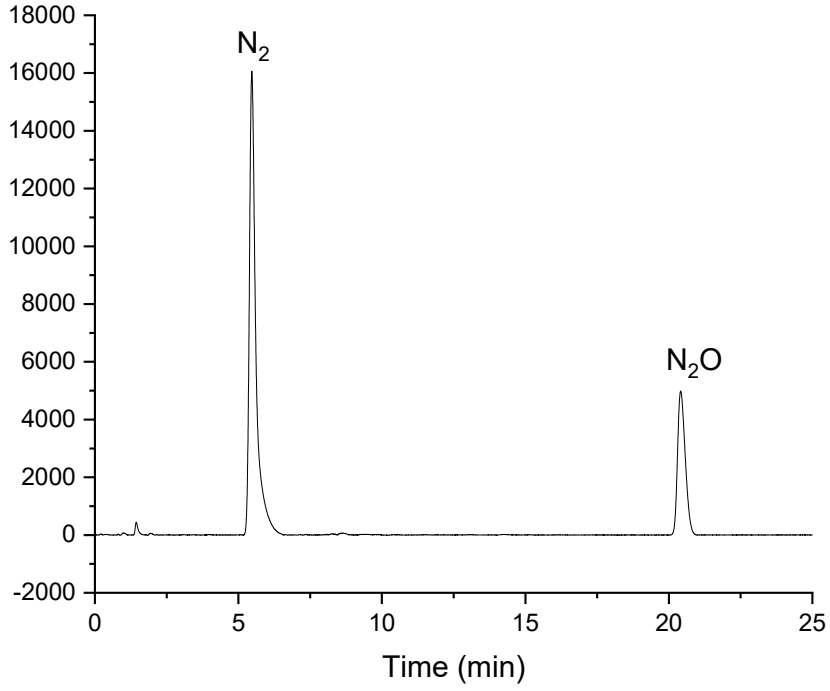

Figure 4.3 GC trace of headspace of 1:1 SmI_2:N_2O reaction.

Experimental observation indicates that in a 1:1 mixture of SmI_2:N_2O a yield of roughly 50% N_2 is observed, with a large amount of N_2O remaining unreacted. When the same experiment is run with 2:1 mixture of SmI_2:N_2O the result is nearly 100% yield of N_2 with concomitant disappearance of signal associated with N_2O (Fig 4.4). This result is expected, as the reduction of N_2O to N_2 requires two electrons and SmI_2 is a one electron donor (equation 4.1).

$$2\,SmI_2 + N_2O \rightarrow\ SmIO + SmI_3 + N_2 \qquad (\mathbf{4.1})$$

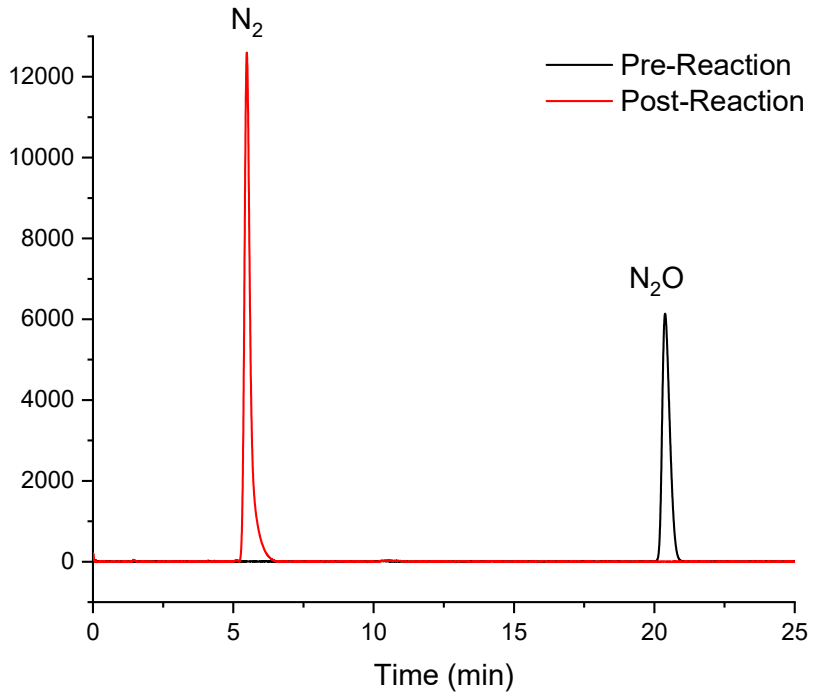

Figure 4.4. GC trace of pre-reaction headspace (black) showing only N_2O and post-reaction headspace (red) showing total conversion to N_2.

The yellow precipitate observed in the reaction was filtered off, washed with THF, dissolved in acetonitrile and layered with diethyl ether, yielding X-ray quality crystals.

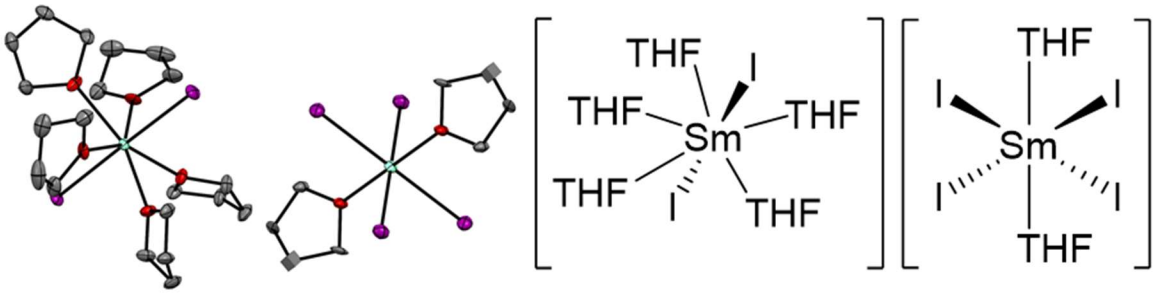

Figure 4.5 $[SmI_4(THF)_2][SmI_2(THF)_5]$ crystal yielded from yellow precipitate.
Left: crystal structure Right: Chemdraw representation

To further elucidate the products UV-Vis spectroscopy was used to characterize both the post-reaction yellow solution and the yellow precipitate (Fig 4.6). The lack of absorbances at 556

and 619 in the post-reaction solutions is a strong indication that all SmI_2 has been consumed. The peaks about 405 cannot be identified at this time, but the peaks about 333 are likely due to SmI_3, which crystalized as $[SmI_4(THF)_2][SmI_2(THF)_5]$.[52] This assertion is supported by the absorption at 340 of the isolated precipitate in MeCN, a mild hypsochromic shift likely due to solvent effects.

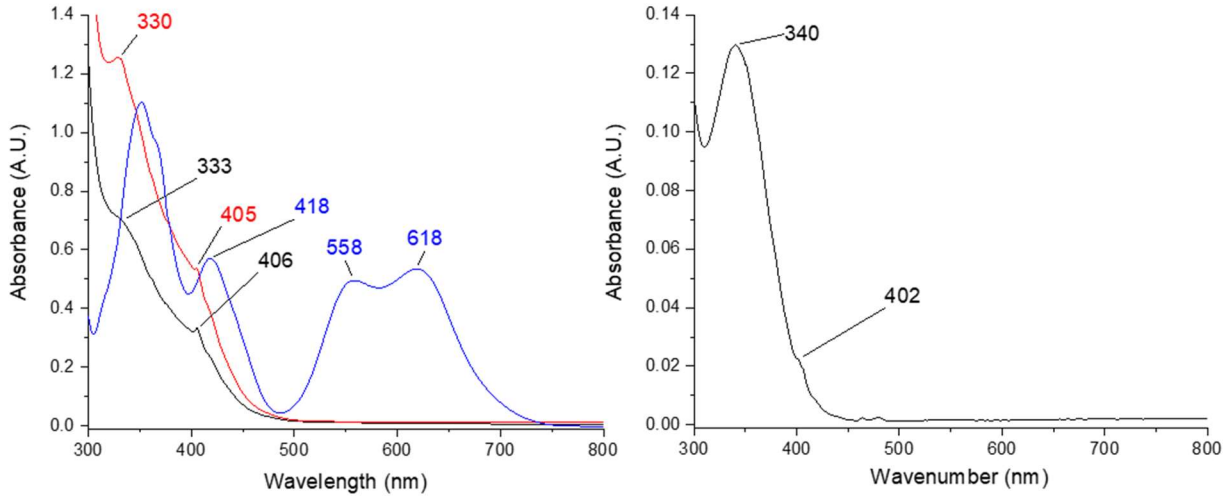

Figure 4.6. UV-Vis comparison of post-reaction yellow solutions in 1:1 (black), 2:1 (red) SmI_2:N_2O reactions and stock SmI_2 (blue) in THF (left). Yellow precipitate in MeCN (right).

To determine the accuracy of equation 4.1 the samarium containing products were examined using mass spectrometry (MS). Samarium has several natural isotopes (Table 4.1.), leading to a distinctive pattern in MS.

Table 4.1: Natural abundance of samarium isotopes

Isotope of Samarium	^{144}Sm	^{147}Sm	^{148}Sm	^{149}Sm	^{150}Sm	^{152}Sm	^{154}Sm
% Abundance	3.083	15.017	11.254	13.83	7.351	26.735	22.73

There multiple regions in the MS data that line up with this distinctive pattern, highlighted in Figure 4.7.

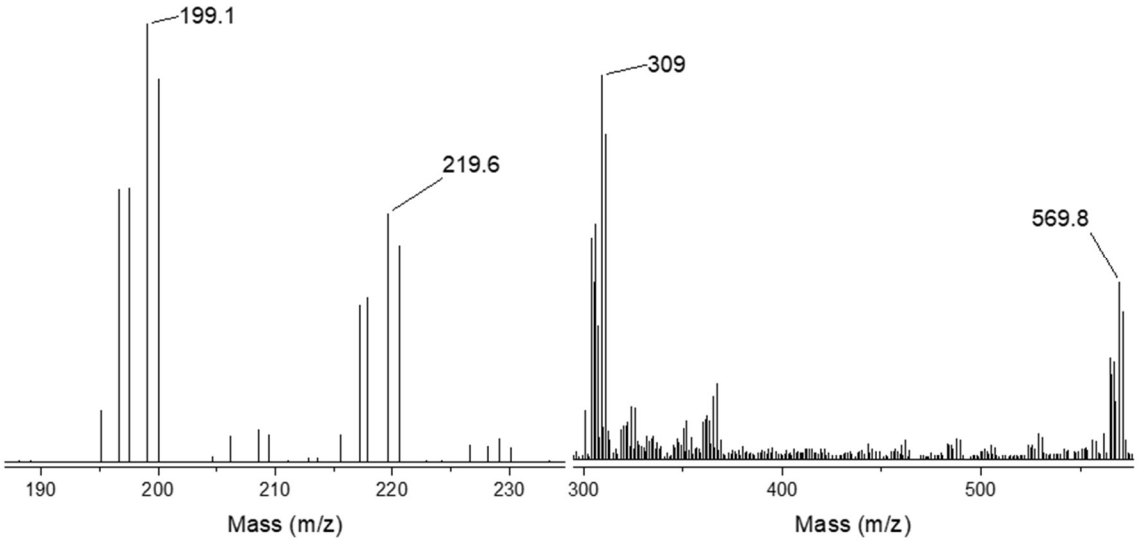

Figure 4.7. Highlighted regions of MS of 2:1 SmI_2:N_2O showing diionized species (left) and singly ionized species (right)

In the highlighted data the peaks at 199.1 and 219.6 can be attributed to doubly ionized SmI·3MeCN and SmI·4MeCN respectively. This corresponds well with the peaks at 309 and 569.8, which are attributed to the singly ionized species SmO·3MeCN·H_2O and SmI_2·4MeCN. This provides some validation that the assignments in equation 4.1 are valid, that a mixture of SmIO and SmI_3 are being generated in the reaction with N_2O.

Chapter 5 – Conclusions

The Co^{Pyrr}PDI system has been shown to reduce nitrite both chemically and electrochemically, though products were not definitively identified. Further work in needed to tune the conditions for electrocatalysis, as well as ensuring that N_2 can be detected to determine if it is a product. A likely primary product if the electrochemical reduction of NO_2^- using the Co^{Pyrr}PDI

system is NH_2OH, though this was not directly detected and shows poor activity in need of optimization. The data indicates that the chemical reduction of NO_2^- using the $Co^{Pyrr}PDI$ forms a Co-NO bond that is labile to vacuum, which should allow for multiple turnovers of reduction reaction, unlike DNIC. Future investigations of the $Co^{Pyrr}PDI$ system will determine the products and mechanisms of NO_2^- reduction.

SmI_2 has been shown to reduce N_2O to N_2 at a 2:1 ratio in 100% yield. Using MS an oxygen containing Sm species was detected, revealing the fate of the O atom in N_2O. While none were proposed here, work is underway to elucidate potential mechanisms, as well as additional nitrogen oxide (NO_x) reductions using SmI_2.

Chapter 6 – Supporting information

6.0 – General Considerations

All reagents were purchased from commercial sources and used as received. Solvents were dried and deoxygenated with a PureSolv solvent purification system. ^{Pyrr}PDI was synthesized according to a literature procedure.[36] Unless otherwise noted all manipulations were carried out in a nitrogen filled glovebox.

6.1 – Synthesis

$Co^{Pyrr}PDI(OTf)_2$. A 20 mL scintillation vial was charged with ^{Pyrr}PDI (0.500 g, 1.194 mmol) and $Co(OTf)_2$ (0.432 g, 1.194 mmol) and a PTFE stir bar and 5 mL of MeCN. The solution was stirred overnight, resulting in a deep red solution. The solution was filtered through celite and layered with diethyl ether resulting in red crystals of $Co^{Pyrr}PDI(OTf)_2$ (0.746 g, 0.961 mmol, 80% yield).

$[CoH^{Pyrr}PDI(CO)I][I]$. In a nitrogen filled glovebox a Fisher Porter tube was charged with a PTFE stir bar, $Co^{Pyrr}PDI(OTf)_2$ (0.250 g, 0.322 mmol) and 4 mL 0.1 M (0.400 mmol) SmI_2

solution in THF. The tube was then sealed, removed from the glovebox and pressurized with 30 psi of CO. The reaction was allowed to stir overnight after which all solvent was removed by vacuum and the tube was returned to the glovebox. The solid was re-dissolved in THF and filtered through celite, and dried under vacuum, and triturated with 15 mL of diethyl ether overnight. The diethyl ether was then decanted and the solid was dissolved in 5 mL MeCN and layered with diethyl ether. This resulted in green crystals of [$CoH^{Pyrr}PDI(CO)I$][I] (0.105 g, 0.138 mmol, 42% yield).

Reduction of NO_2^- with [$CoH^{Pyrr}PDI(CO)I$][I].

An oven dried 25 mL sidearm reaction tube was charged with a PTFE stir bar, [$CoH^{Pyrr}PDI(CO)I$][I] (0.050 g, 0.066 mmol) and $TBANO_2$ (0.019 g, 0.066 mmol). To this tube 10 mL of MeCN was added, the tube was sealed, stirring was turned on and the reaction was allowed to proceed overnight. The resulting red solution was analyzed by gas and liquid phase IR before being filtered through celite. The solvent was then removed by vacuum and condensed phase IR was gathered. The solid was then triturated with pentane before being dissolved in acetonitrile and layered with diethyl ether. This resulted in a non-crystalline solid that could not be definitively identified.

Reduction of CO_2 with $Co^{Pyrr}PDI(OTf)_2$.

In a nitrogen filled glovebox an oven dried 25 mL sidearm reaction tube was charged with a PTFE stir bar, $Co^{Pyrr}PDI(OTf)_2$ (0.250 g, 0.322 mmol) and 0.1 M SmI_2 solution in THF (6.4 mL, 0.640 mmol). The vessel was sealed with a PTFE plug and the sidearm sealed with a rubber Suba-Seal® septa. This tube was then removed from the glovebox and CO_2 (0.014 mL, 0.322 mmol) was introduced via gastight syringe. The resulting red solution was analyzed by gas and liquid phase before being filtered through celite. The solvent was then removed by vacuum and condensed

phase IR was gathered. The solid was then triturated with pentane before being dissolved in acetonitrile and layered with diethyl ether. This resulted in a non-crystalline solid that could not be definitively identified.

Reduction of N_2O with SmI_2. To an oven dried 25 mL side arm reaction tube charged with a PTFE stir bar 5 mL of SmI_2 solution in THF was added. The vessel was sealed with a PTFE plug and the sidearm sealed with a rubber Suba-Seal® septa. The solution was then degassed by three consecutive rounds of freeze pump thaw. N_2O (one or two mole equivalent relative to SmI_2, concentration verified via UV-Vis spectroscopy) was then layered onto the frozen THF at 77 K. The vessel was then allowed to warm and stirred for two days after which the solution had turned from deep blue to pale yellow.

6.2 – NMR Spectra

NMR spectra were collected on a Bruker 500 MHz Ft-NMR spectrometer. Data are reported in ppm referenced to TMS.

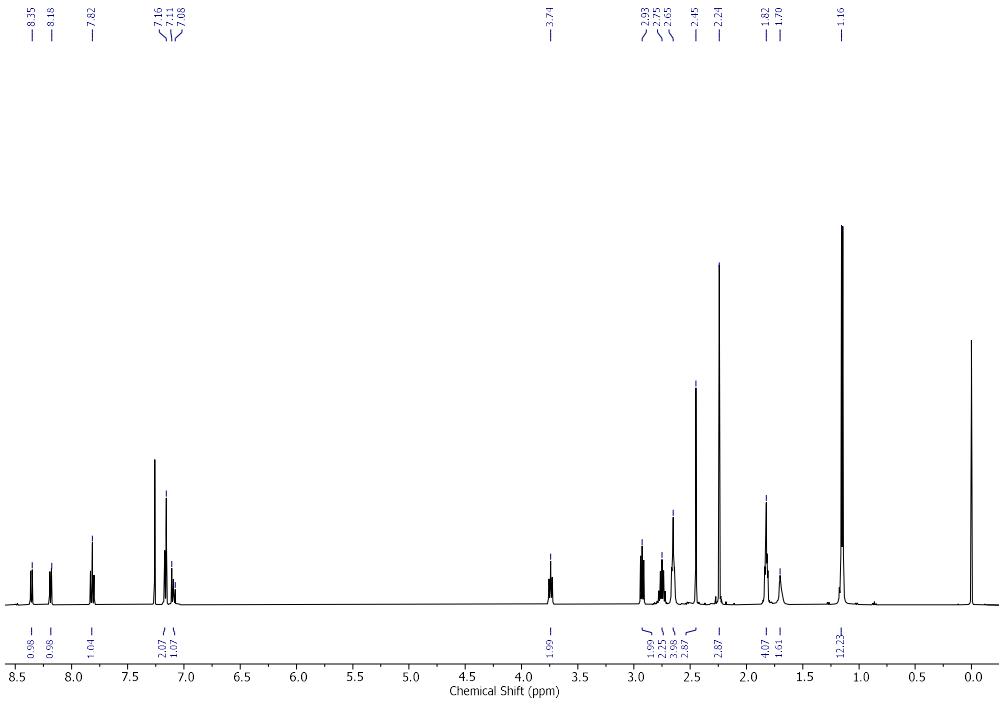

Figure 6.1. ^1H NMR of ^{Pyrr}PDI ligand

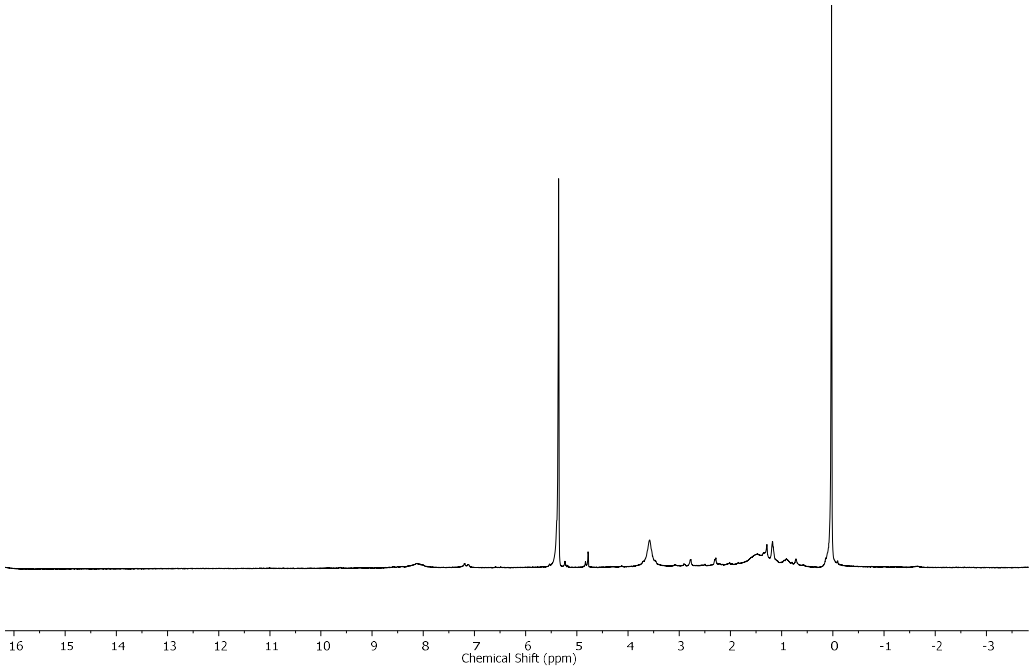

Figure 6.2. ^{1}H NMR of [CoH^{Pyrr}PDI(CO)I][I]

6.3 – FT-IR Spectra

IR spectra were collected on a Thermo Scientific Nicolet iS10 FT-IR spectrometer. Solid phase samples were analyzed using an ATR accessory. Solution phase samples were analyzed using a transmission accessory and a liquid IR cell equipped with CaF_2 salt plates. Gas phase samples were analyzed using a transmission accessory and a 100 mm path length gas IR cell equipped with NaCl salt plates.

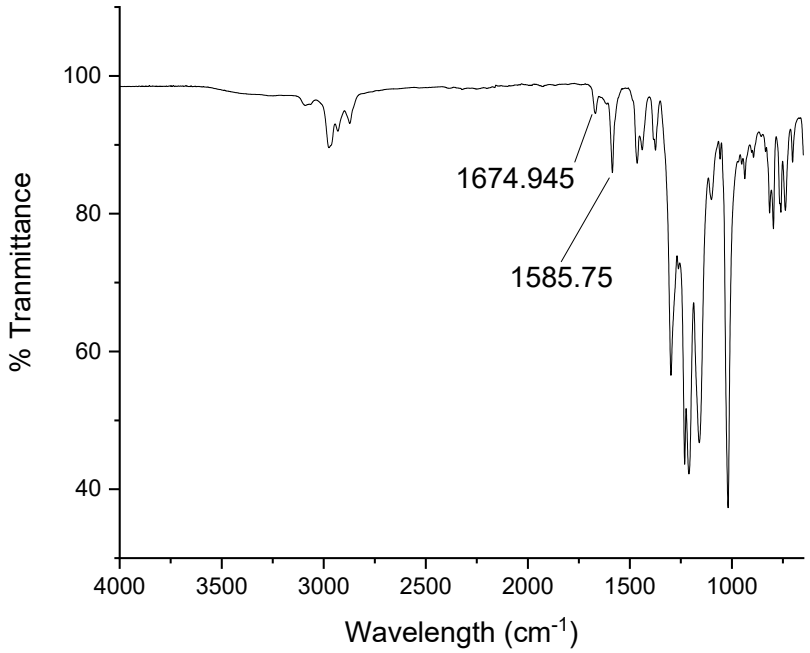

Figure 6.3. Condensed phase IR of $Co^{Pyrr}PDI(OTf)_2$

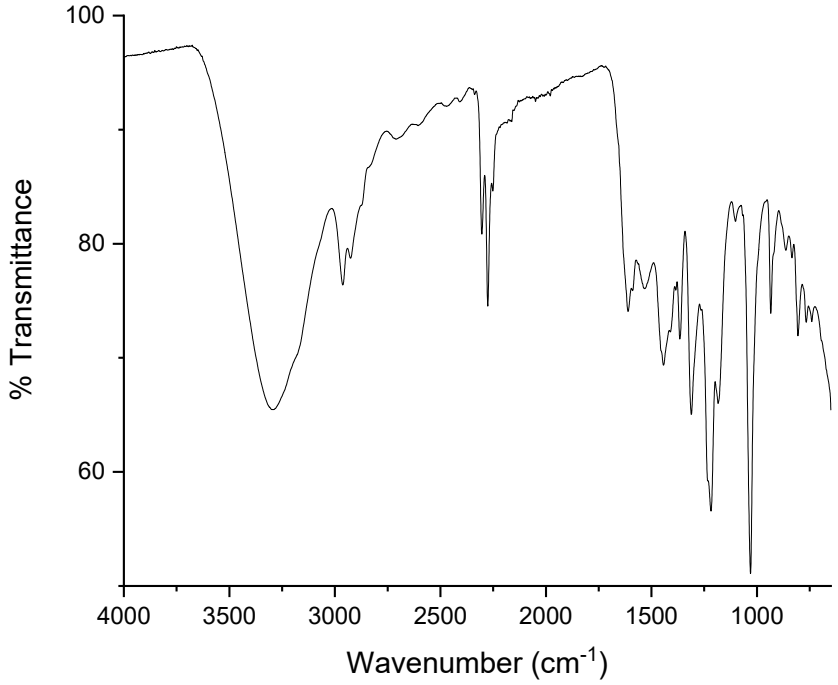

Figure 6.4. Condensed phase IR of oil of $Co^{Pyrr}PDI(OTf)_2$ post CO_2 reduction

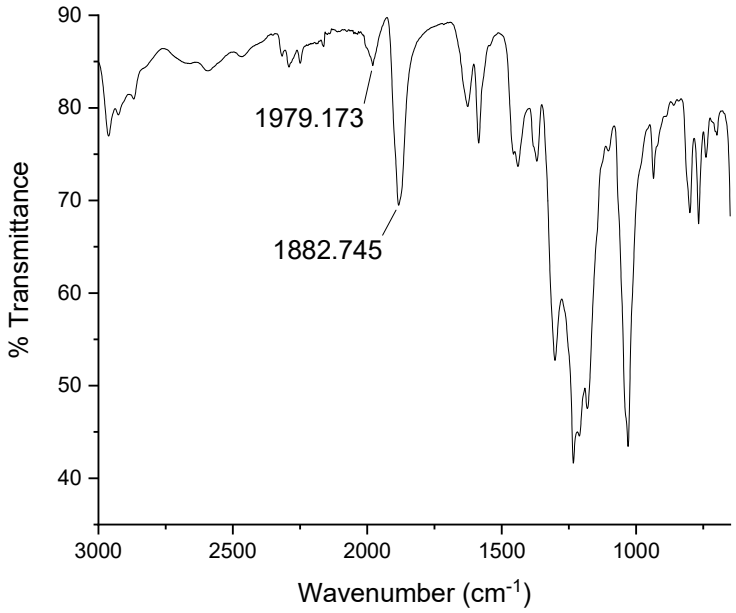

Figure 6.5. Condensed phase IR of [CoH^{Pyrr}PDI(CO)I][I].

6.4 – UV-Vis spectra

All UV-Vis spectra were collected using a Jasco V-670 UV/Vis and 1 cm path length quartz UV-Vis cells from Starna Cells.

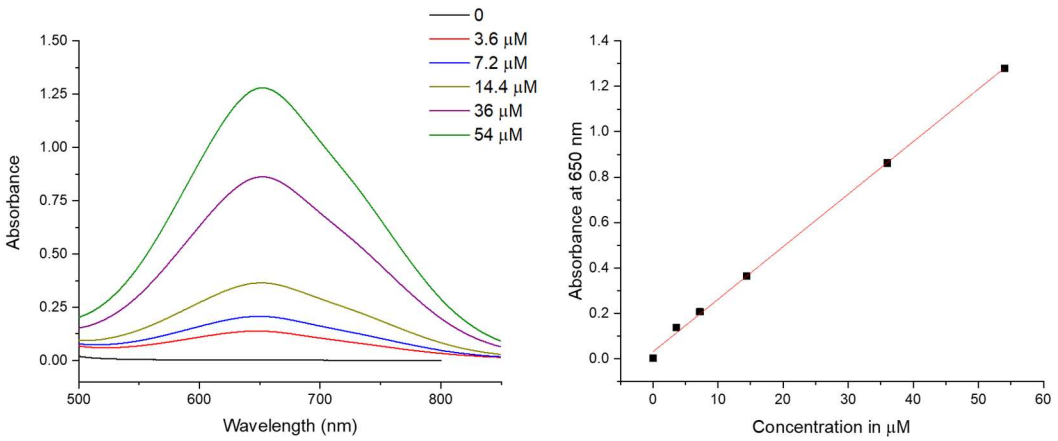

Figure 6.6. Calibration data for ammonium colorimetric testing of ammonium[41]. Slope: 0.02276 ± 0.0002 Intercept: 0.04592 ± 0.006 R^2: 0.999 Calibration concentrations generated using 0.0019 M stock solution of NH_4PF_6

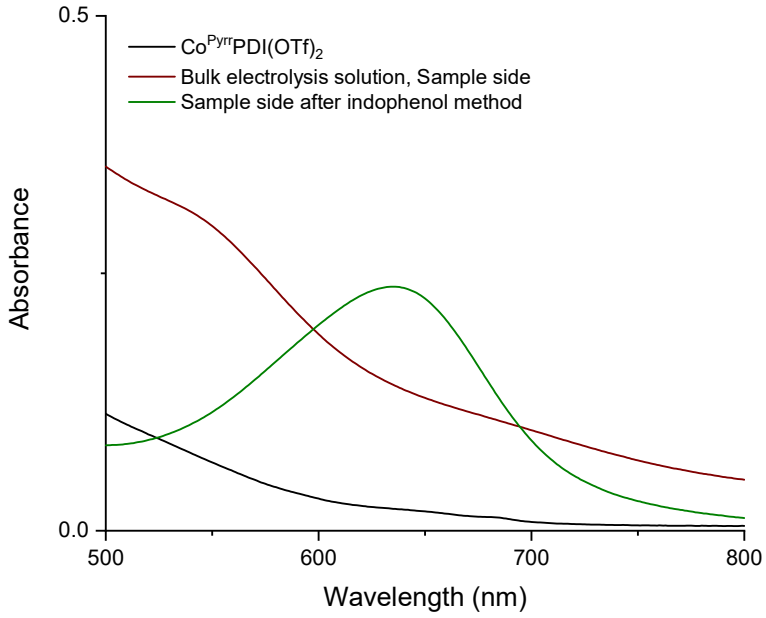

Figure 6.7. Comparison of UV-Vis spectra of $Co^{Pyrr}PDI(OTf)_2$ (black), electrolysis solution post BE (red) and electrolysis solution post BE treated with indophenol method to test for ammonia showing 10 µM concentration, 19% faradaic yield (green).

6.5 – MS Spectra

MS spectra were collected using an Advion CMS expression^{L} mass spectrometer. Samples were prepared in MeCN and directly infused into the mass spectrometer using MeCN as a carrier at 0.3 mL/min. Data was analyzed using Advion Data Express software package.

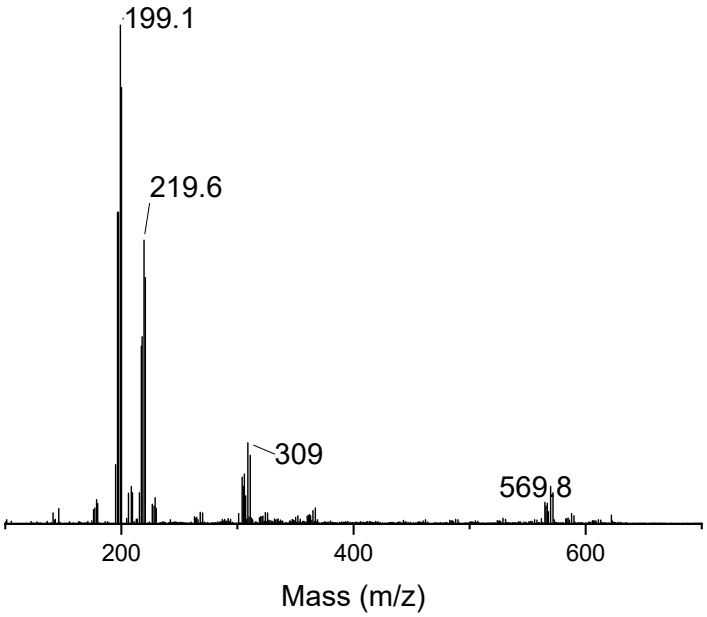

Figure 6.8. MS of 1:1 SmI_2:N_2O

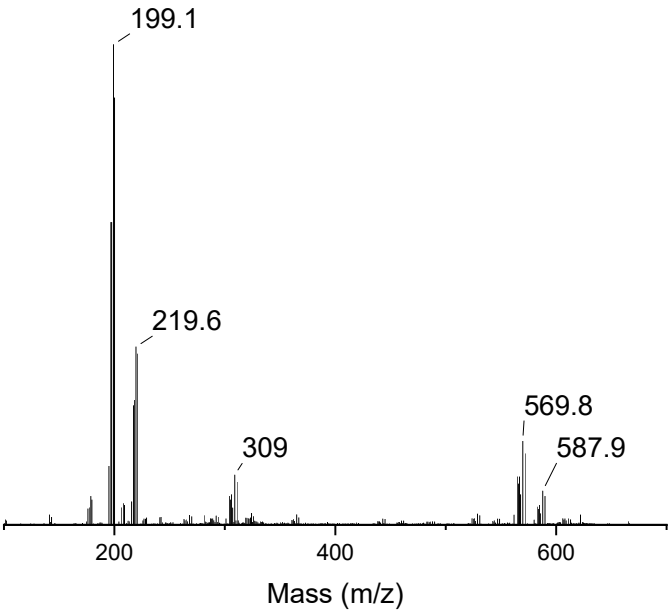

Figure 6.9. MS of 2:1 SmI_2:N_2O

6.6 – GC chromatographs

GC chromatographs were collected on an SRI 8610C gas chromatograph equipped with a 10 foot, 2mm inner diameter Carbonex-1000 column. Unless otherwise noted the heating profile used was 30 °C for 8 minutes followed by a ramp of 20 °C to 200 °C, which is held for 12 minutes.

Single point calibration was used for quantification of gases. For each reaction a control for calibration purposes was set up in parallel as follows; a 25 mL sidearm reaction tube was charged with 5 mL of THF and a PTFE stir bar, then subjected to three rounds of freeze-pump-thaw and the same volume of N_2 was introduced as N_2O in the reaction being controlled for.

6.7 – Voltammetry

Voltammetry was carried out using a Pine Wavenow potentiostat. Unless otherwise noted all voltammetry was done in MeCN with 0.1 M $TBAPF_6$ as an electrolyte.

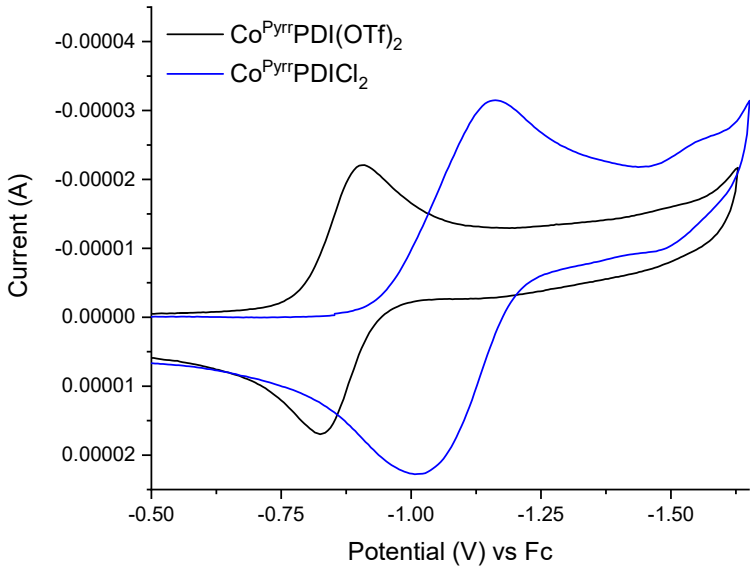

Figure 6.10. Comparison of first reductive event of $Co^{Pyrr}PDI(OTf)_2$ and $Co^{Pyrr}PDICl_2$

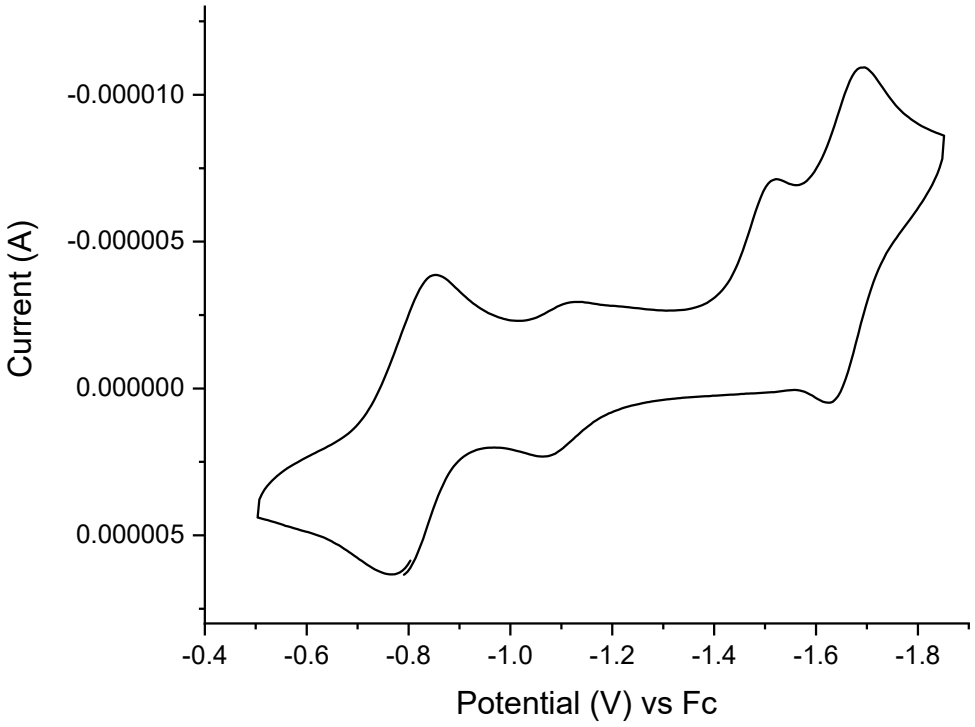

Figure 6.11. CV of [CoH^{Pyrr}PDI(CO)I][I]

6.8 – Crystallographic Data

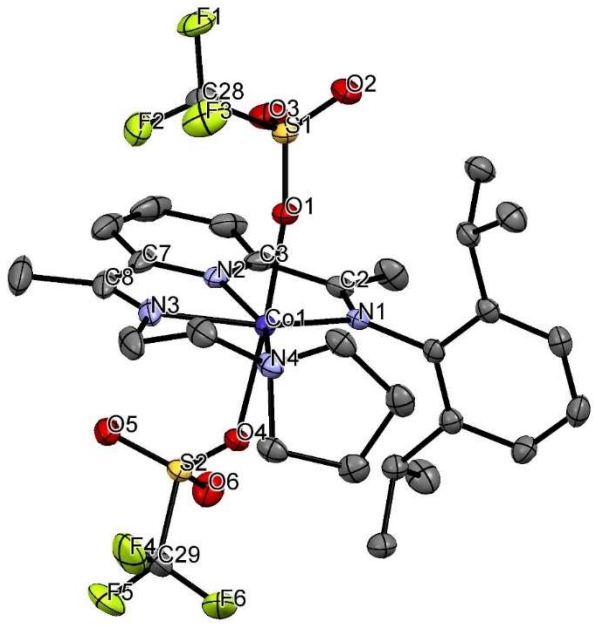

Figure 6.12. ORTEP representation of crystal structure of $Co^{Pyrr}PDI(OTf)_2$. Selected bond lengths (Å): Co(1) - O(4), 2.196(1); Co(1) - O(1), 2.180(1); Co(1) - N(1), 2.197(1); Co(1) - N(2), 2.048(2); Co(1) - N(3), 2.093(2) ; Co(1) - N(4), 2.160(2); N(1) - C(2), 1.289(2); N(3) - C(8), 1.268(3); C(2) - C(3), 1.493(2); C(7) - C(8), 1.493(4)

X-ray diffraction data for $[CoH^{Pyrr}PDI(CO)I][I]$ were collected at 100 K on a Bruker D8 Venture using MoKα-radiation (λ=0.71073 Å). Data have been corrected for absorption using SADABS area detector absorption correction program. Using Olex2, the structure was solved with the SHELXT structure solution program using Direct Methods and refined with the SHELXL refinement package using least squares minimization. All non-hydrogen atoms were refined with anisotropic thermal parameters. The hydrogen atom of the pyrrolidine nitrogen was found from the difference map, placed and refined. The remaining hydrogen atoms of the investigated structure were located from difference Fourier maps but finally their positions were placed in geometrically calculated positions and refined using a riding model. Isotropic thermal parameters of the placed hydrogen atoms were fixed to 1.2 times the *U* value of the atoms they are linked to (1.5 times for methyl groups). Calculations and refinement of structures were carried out using APEX3, SHELXTL, and Olex2 software.

Additional refinement details:

The structure was found to be a two component non-merohedral twin. The twin law found by the TwinRotMat routine within PLATON was found to 0.998, 0.003. 0.003, 0.499, -0.999, 0.001, 0.999 0.002, -0.998. Refinement of HKLF5 data with SHELXL resulted in a BASF of 0.3586(10). During structure refinement it became evident that substitutional disorder was likely present. Specifically, when the complex is modeled with only a carbonyl ligand there is excess electron density around the carbonyl oxygen, and insufficient electron density at the carbonyl carbon site. Considering the axial ligand is iodide, and the previous reaction to obtain the complex was with SmI_2, it would seem plausible that some amount of a di-iodide cobalt complex is present, which would account for the observations previously stated. Therefore, the disorder is modeled as substitutional disorder and required the use of bond length and thermal ellipsoid restraints to obtain a reasonable stable for refinement. The disorder also accounts for the non-integer values found in the chemical/unit cell formulas.

Crystallographic Data for $[CoH^{Pyrr}PDI(CO)I][I]$ $C_{27.89}H_{39}CoI_{2.11}N_4O_{0.89}$ (M =771.24 g/mol): triclinic, space group P-1 (no. 2), a = 8.3626(7) Å, b = 8.5420(7) Å, c = 22.9761(18) Å, α = 81.298(2)°, β = 79.792(2)°, γ = 75.949(2)°, V = 1556.8(2) Å^3, Z = 2, T = 100 K, μ(MoKα) = 2.669 mm^{-1}, *Dcalc* = 1.645 g/cm^3, 2Θmax = 50.26°, 5523 reflections measured, 5523 unique (R_{sigma} = 0.0266), R_1 = 0.0375 (I > 2σ(I)), wR_2 = 0.0889 (all data).

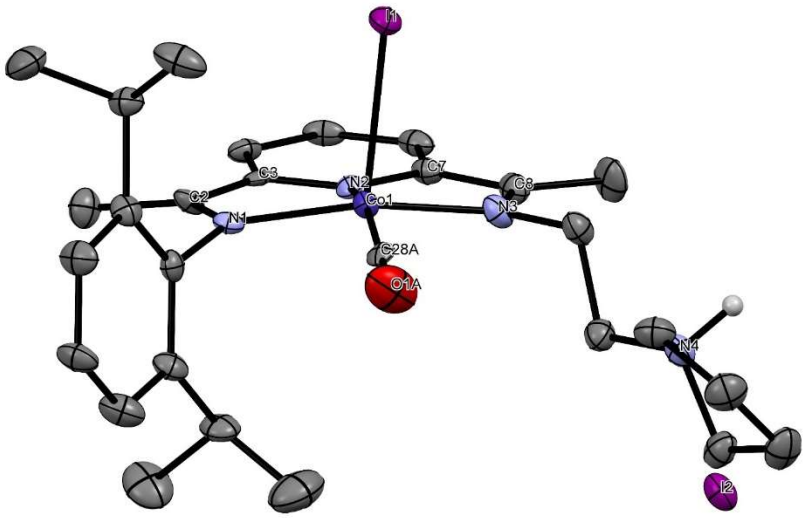

Figure 6.13. ORTEP representation of crystal structure of [CoH^{Pyrr}PDI(CO)I][I]. Selected bond lengths (Å): Co(1) - I(1), 2.6519(9); Co(1) - N(1), 1.937(5); Co(1) - N(2), 1.843(6); Co(1) - N(3), 1.942(4) ; Co(1) - C(28A), 1.789(8); N(1) - C(2), 1.317(9); N(3) - C(8), 1.31(1); C(2) - C(3), 1.44(1); C(7) - C(8), 1.446(9); C(28A) - O(1A), 1.15(2)

Data collections on yellow crystals of $[SmI_4(THF)_2][SmI_2(THF)_5]$ was first undertaken by securing single crystals with dimensions of 0.53 x 0.38 x 0.15 mm^3 to Mitegen mounts using Paratone oil. Those crystals were then mounted on a Rigaku Oxford Diffraction (ROD) XtaLABPRO equipped with a Pilatus P200K hybrid photon counting (HPC) detector and fine-focused Mo $K_{\alpha 1}$ radiation (= 0.71073 Å). Reflection data was collected at 100 K with data collection strategies to ensure completeness and desired redundancy determined using CrysAlis^{Pro}. Data processing for all samples was done using CrysAlis^{Pro} and included numerical absorption corrections applied via face-indexing using the SCALE3 ABSPACK scaling algorithm. All structures were solved via intrinsic phasing methods using ShelXT and subjected to a least-squares refinement with ShelXL within the Olex2 graphical user interface. The final structural refinement included anisotropic temperature factors on all constituent non-hydrogen atoms. Hydrogen atoms were attached via the riding model at calculated positions using suitable HFIX commands. Space groups were

unambiguously verified by PLATON. As a means to achieve reasonable bond distances and thermal parameters within the structural model RIGU constraints and restraints were used

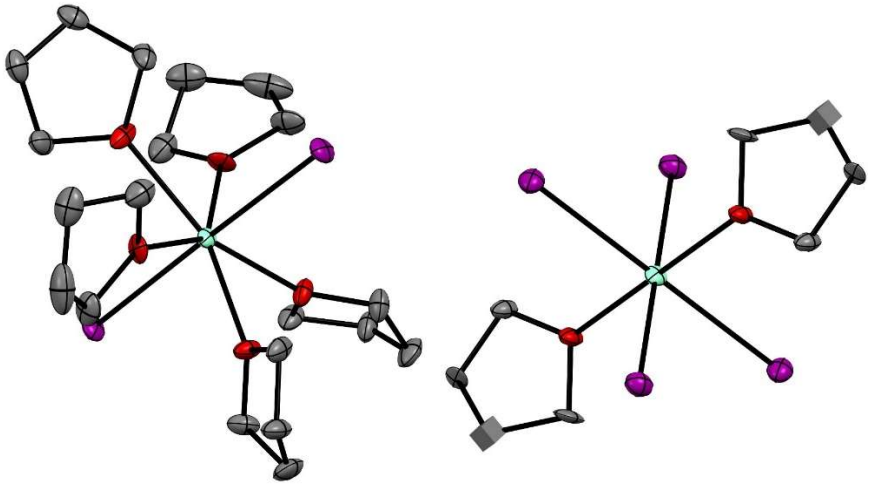

Figure 6.14. ORTEP representation of crystal structure of $[SmI_4(THF)_2][SmI_2(THF)_5]$. Sm-Sm distance: 9.401 Å

Works Cited

(1) Meyer, F.; Tolman, W. B. Forums on Small-Molecule Activation: From Biological Principles to Energy Applications. *Inorg. Chem.* **2015**, *54*, 5039–5039. https://doi.org/10.1021/acs.inorgchem.5b00768.

(2) Porosoff, M. D.; Yan, B.; Chen, J. G. Catalytic Reduction of CO2 by H2 for Synthesis of CO, Methanol and Hydrocarbons: Challenges and Opportunities. *Energy Environ. Sci.* **2016**, *9*, 62–73. https://doi.org/10.1039/C5EE02657A.

(3) *Ammonia*; Nielsen, A., Ed.; Springer Berlin Heidelberg: Berlin, Heidelberg, 1995. https://doi.org/10.1007/978-3-642-79197-0.

(4) Erisman, J. W.; Sutton, M. A.; Galloway, J.; Klimont, Z.; Winiwarter, W. How a Century of Ammonia Synthesis Changed the World. *Nat. Geosci.* **2008**, *1*, 636–639. https://doi.org/10.1038/ngeo325.

(5) Bykov, D.; Neese, F. Six-Electron Reduction of Nitrite to Ammonia by Cytochrome *c* Nitrite Reductase: Insights from Density Functional Theory Studies. *Inorg. Chem.* **2015**, *54*, 9303–9316. https://doi.org/10.1021/acs.inorgchem.5b01506.

(6) Diaz, R. J.; Rosenberg, R. Spreading Dead Zones and Consequences for Marine Ecosystems. *Science* **2008**, *321*, 926–929. https://doi.org/10.1126/science.1156401.

(7) McEvoy, J. P.; Brudvig, G. W. Water-Splitting Chemistry of Photosystem II. *Chem. Rev.* **2006**, *106*, 4455–4483. https://doi.org/10.1021/cr0204294.

(8) Himo, F.; Eriksson, L. A.; Maseras, F.; Siegbahn, P. E. M. Catalytic Mechanism of Galactose Oxidase: A Theoretical Study. *J. Am. Chem. Soc.* **2000**, *122*, 8031–8036. https://doi.org/10.1021/ja994527r.

(9) Whittaker, M. M.; Whittaker, J. W. Catalytic Reaction Profile for Alcohol Oxidation by Galactose Oxidase. *Biochemistry* **2001**, *40* (24), 7140–7148. https://doi.org/10.1021/bi010303l.

(10) Whittaker, J. W. The Radical Chemistry of Galactose Oxidase. *Arch. Biochem. Biophys.* **2005**, *433*, 227–239. https://doi.org/10.1016/j.abb.2004.08.034.

(11) Babcock, G. T.; El-Deeb, M. K.; Sandusky, P. O.; Whittaker, M. M.; Whittaker, J. W. Electron Paramagnetic Resonance and Electron Nuclear Double Resonance Spectroscopies of the Radical Site in Galactose Oxidase and of Thioether-Substituted Phenol Model Compounds. *J. Am. Chem. Soc.* **1992**, *114*, 3727–3734. https://doi.org/10.1021/ja00036a023.

(12) Whittaker, J. W. Free Radical Catalysis by Galactose Oxidase. *Chem. Rev.* **2003**, *103,* 2347–2364. https://doi.org/10.1021/cr020425z.

(13) Gerfen, G. J.; Bellew, B. F.; Griffin, R. G.; Singel, D. J.; Ekberg, C. A.; Whittaker, J. W. High-Frequency Electron Paramagnetic Resonance Spectroscopy of the Apogalactose Oxidase Radical. *J. Phys. Chem.* **1996**, *100*, 16739–16748. https://doi.org/10.1021/jp960709l.

(14) Rokhsana, D.; Howells, A. E.; Dooley, D. M.; Szilagyi, R. K. Role of the Tyr-Cys Cross-Link to the Active Site Properties of Galactose Oxidase. *Inorg. Chem.* **2012**, *51*, 3513–3524. https://doi.org/10.1021/ic2022769.

(15) Warren, J. J.; Mayer, J. M. Moving Protons and Electrons in Biomimetic Systems. *Biochemistry* **2015**, *54*, 1863–1878. https://doi.org/10.1021/acs.biochem.5b00025.

(16) Drummond, M. J.; Ford, C. L.; Gray, D. L.; Popescu, C. V.; Fout, A. R. Radical Rebound Hydroxylation Versus H-Atom Transfer in Non-Heme Iron(III)-Hydroxo Complexes: Reactivity and Structural Differentiation. *J. Am. Chem. Soc.* **2019**, *141*, 6639–6650. https://doi.org/10.1021/jacs.9b01516.

(17) Meunier, B.; de Visser, S. P.; Shaik, S. Mechanism of Oxidation Reactions Catalyzed by Cytochrome P450 Enzymes. *Chem. Rev.* **2004**, *104*, 3947–3980. https://doi.org/10.1021/cr020443g.

(18) Ford, C. L.; Park, Y. J.; Matson, E. M.; Gordon, Z.; Fout, A. R. A Bioinspired Iron Catalyst for Nitrate and Perchlorate Reduction. *Science* **2016**, *354*, 741–743. https://doi.org/10.1126/science.aah6886.

(19) Miller, A. J. M. Controlling Ligand Binding for Tunable and Switchable Catalysis: Cation-Modulated Hemilability in Pincer-Crown Ether Ligands. *Dalton Trans.* **2017**, *46*, 11987–12000. https://doi.org/10.1039/C7DT02156A.
(20) Jeffrey, J. C.; Rauchfuss, T. B. Metal Complexes of Hemilabile Ligands. Reactivity and Structure of Dichlorobis(o-(Diphenylphosphino)Anisole)Ruthenium(II). *Inorg. Chem.* **1979**, *18*, 2658–2666. https://doi.org/10.1021/ic50200a004.
(21) Slone, C. S.; Weinberger, D. A.; Mirkin, C. A. The Transition Metal Coordination Chemistry of Hemilabile Ligands. In *Progress in Inorganic Chemistry*; Karlin, K. D., Ed.; John Wiley & Sons, Inc.: Hoboken, NJ, USA, 2007; pp 233–350. https://doi.org/10.1002/9780470166499.ch3.
(22) Lindner, R.; van den Bosch, B.; Lutz, M.; Reek, J. N. H.; van der Vlugt, J. I. Tunable Hemilabile Ligands for Adaptive Transition Metal Complexes. *Organometallics* **2011**, *30*, 499–510. https://doi.org/10.1021/om100804k.
(23) Braunstein, P.; Naud, F. Hemilability of Hybrid Ligands and the Coordination Chemistry of Oxazoline-Based Systems. *Angew. Chem. Int. Ed.* **2001**, *40*, 680–699. https://doi.org/10.1002/1521-3773(20010216)40:4<680::AID-ANIE6800>3.0.CO;2-0.
(24) Bischoff, S.; Weigt, A.; Miessner, H.; Lücke, B. Hemilabile Phosphonate−Phosphane−Rh Catalysts for Homogeneous and Heterogeneous Carbonylation. *Energy Fuels* **1996**, *10*, 520–523. https://doi.org/10.1021/ef950170a.
(25) Baumgardner, D. F.; Parks, W. E.; Gilbertson, J. D. Harnessing the Active Site Triad: Merging Hemilability, Proton Responsivity, and Ligand-Based Redox-Activity. *Dalton Trans.* **2020**, *4*, 960-965. https://doi.org/10.1039/C9DT04470A.
(26) Weng, Z.; Teo, S.; Hor, T. S. A. Metal Unsaturation and Ligand Hemilability in Suzuki Coupling. *Acc. Chem. Res.* **2007**, *40*, 676–684. https://doi.org/10.1021/ar600003h.
(27) Lyaskovskyy, V.; de Bruin, B. Redox Non-Innocent Ligands: Versatile New Tools to Control Catalytic Reactions. *ACS Catal.* **2012**, *2*, 270–279. https://doi.org/10.1021/cs200660v.
(28) Manna, C. M.; Kaur, A.; Yablon, L. M.; Haeffner, F.; Li, B.; Byers, J. A. Stereoselective Catalysis Achieved through in Situ Desymmetrization of an Achiral Iron Catalyst Precursor. *J. Am. Chem. Soc.* **2015**, *137*, 14232–14235. https://doi.org/10.1021/jacs.5b09966.
(29) Mukhopadhyay, T. K.; Flores, M.; Groy, T. L.; Trovitch, R. J. A Highly Active Manganese Precatalyst for the Hydrosilylation of Ketones and Esters. *J. Am. Chem. Soc.* **2014**, *136*, 882–885. https://doi.org/10.1021/ja4116346.
(30) Kwon, Y. M.; Delgado, M.; Zakharov, L. N.; Seda, T.; Gilbertson, J. D. Nitrite Reduction by a Pyridinediimine Complex with a Proton-Responsive Secondary Coordination Sphere. *Chem. Commun.* **2016**, *52*, 11016–11019. https://doi.org/10.1039/C6CC05962G.
(31) Ye, S.; Neese, F. The Unusual Electronic Structure of Dinitrosyl Iron Complexes. *J. Am. Chem. Soc.* **2010**, *132*, 3646–3647. https://doi.org/10.1021/ja9091616.
(32) Guo, Y.; Stroka, J. R.; Kandemir, B.; Dickerson, C. E.; Bren, K. L. Cobalt Metallopeptide Electrocatalyst for the Selective Reduction of Nitrite to Ammonium. *J. Am. Chem. Soc.* **2018**, *140*, 16888–16892. https://doi.org/10.1021/jacs.8b09612.
(33) Taniguchi, I.; Nakashima, N.; Matsushita, K.; Yasukouchi, K. Electrocatalytic Reduction of Nitrate and Nitrite to Hydroxylamine and Ammonia Using Metal Cyclams. *J. Electroanal. Chem. Interfacial Electrochem.* **1987**, *224*, 199–209. https://doi.org/10.1016/0022-0728(87)85092-1.
(34) Thammavongsy, Z.; Seda, T.; Zakharov, L. N.; Kaminsky, W.; Gilbertson, J. D. Ligand-Based Reduction of CO_2 and Release of CO on Iron(II). *Inorg. Chem.* **2012**, *51*, 9168–9170. https://doi.org/10.1021/ic3015404.
(35) Evans, W. J.; Grate, J. W.; Bloom, I.; Hunter, W. E.; Atwood, J. L. Synthesis and X-Ray Crystallographic Characterization of an Oxo-Bridged Bimetallic Organosamarium Complex, [(C5Me5)2Sm]2(.Mu.-O). *J. Am. Chem. Soc.* **1985**, *107*, 405–409. https://doi.org/10.1021/ja00288a021.
(36) Cheung, P. M.; Burns, K. T.; Kwon, Y. M.; Deshaye, M. Y.; Aguayo, K. J.; Oswald, V. F.; Seda, T.; Zakharov, L. N.; Kowalczyk, T.; Gilbertson, J. D. Hemilabile Proton Relays and Redox

Activity Lead to {FeNO}^{x} and Significant Rate Enhancements in NO_2^- Reduction. *J. Am. Chem. Soc.* **2018**, *140*, 17040–17050. https://doi.org/10.1021/jacs.8b08520.
(37) Elgrishi, N.; Rountree, K. J.; McCarthy, B. D.; Rountree, E. S.; Eisenhart, T. T.; Dempsey, J. L. A Practical Beginner's Guide to Cyclic Voltammetry. *J. Chem. Educ.* **2018**, *95*, 197–206. https://doi.org/10.1021/acs.jchemed.7b00361.
(38) Thammavongsy, Z.; LeDoux, M. E.; Breuhaus-Alvarez, A. G.; Seda, T.; Zakharov, L. N.; Gilbertson, J. D. Pyridinediimine Iron Dicarbonyl Complexes with Pendant Lewis Bases and Lewis Acids Located in the Secondary Coordination Sphere. *Eur. J. Inorg. Chem.* **2013**, *2013*, 4008–4015. https://doi.org/10.1002/ejic.201300376.
(39) Thamae, M.; Nyokong, T. Cobalt(II) Porphyrazine Catalysed Reduction of Nitrite. *J. Electroanal. Chem.* **1999**, *470* (2), 126–135. https://doi.org/10.1016/S0022-0728(99)00224-7.
(40) Cheng, S.-H.; Su, Y. O. Electrocatalysis of Nitric Oxide Reduction by Water-Soluble Cobalt Porphyrin. Spectral and Electrochemical Studies. *Inorg. Chem.* **1994**, *33*, 5847–5854. https://doi.org/10.1021/ic00103a037.
(41) Weatherburn, M. W. Phenol-Hypochlorite Reaction for Determination of Ammonia. *Anal. Chem.* **1967**, *39*, 971–974. https://doi.org/10.1021/ac60252a045.
(42) Bowman, A. C.; Milsmann, C.; Hojilla Atienza, C. C.; Lobkovsky, E.; Wieghardt, K.; Chirik, P. J. Synthesis and Molecular and Electronic Structures of Reduced Bis(Imino)Pyridine Cobalt Dinitrogen Complexes: Ligand versus Metal Reduction. *J. Am. Chem. Soc.* **2010**, *132*, 1676–1684. https://doi.org/10.1021/ja908955t.
(43) Lashof, D. A.; Ahuja, D. R. Relative Contributions of Greenhouse Gas Emissions to Global Warming. *Nature* **1990**, *344* (6266), 529–531. https://doi.org/10.1038/344529a0.
(44) Scheehle, E. A.; Kruger, D. Global Anthropogenic Methane and Nitrous Oxide Emissions. *Energy J.* **2006**, *27*, 33–44.
(45) Ebert, H.; Parsons, R.; Ritzoulis, G.; VanderNoot, T. The Reduction of Nitrous Oxide on Platinum Electrodes in Acid Solution. *J. Electroanal. Chem. Interfacial Electrochem.* **1989**, *264*, 181–193. https://doi.org/10.1016/0022-0728(89)80156-1.
(46) Johnson, K. E.; Sawyer, D. T. The Electrochemical Reduction of Nitrous Oxide in Alkaline Solution. *J. Electroanal. Chem. Interfacial Electrochem.* **1974**, *49*, 95–103. https://doi.org/10.1016/S0022-0728(74)80349-9.
(47) Borkó, L.; Vlasenko, N. V.; Koppány, Zs.; Beck, A.; Puziy, A. M. Effect of Redox and Acid Properties of Ga–H-ZSM-5 Nanophase Catalysts Modified by Transition Metals on the Reduction of Nitrous Oxide by Methane. *Theor. Exp. Chem.* **2018**, *54*, 247–254. https://doi.org/10.1007/s11237-018-9570-x.
(48) Kagan, H. B.; Namy, J. L. Chapter 50 Preparation of Divalent Ytterbium and Samarium Derivatives and Their Use in Organic Chemistry. In *Handbook on the Physics and Chemistry of Rare Earths*; Elsevier, 1984; Vol. 6, pp 525–565. https://doi.org/10.1016/S0168-1273(84)06007-4.
(49) Szostak, M.; Spain, M.; Procter, D. J. Recent Advances in the Chemoselective Reduction of Functional Groups Mediated by Samarium(II) Iodide: A Single Electron Transfer Approach. *Chem. Soc. Rev.* **2013**, *42*, 9155–9183. https://doi.org/10.1039/C3CS60223K.
(50) Sahloul, K.; Sun, L.; Requet, A.; Chahine, Y.; Mellah, M. A Samarium "Soluble" Anode: A New Source of SmI2 Reagent for Electrosynthetic Application. *Chem. – Eur. J.* **2012**, *18*, 11205–11209. https://doi.org/chirik.
(51) Zhang, Y.-F.; Mellah, M. Convenient Electrocatalytic Synthesis of Azobenzenes from Nitroaromatic Derivatives Using SmI_2. *ACS Catal.* **2017**, *7*, 8480–8486. https://doi.org/10.1021/acscatal.7b02940.
(52) Xie, Z.; Chiu, K.; Wu, B.; Mak, T. C. W. Autoionization of SmI3 in Tetrahydrofuran. X-Ray Crystal Structure of the Ionic Complex [SmI2(THF)5][SmI4(THF)2]. *Inorg. Chem.* **1996**, *35*, 5957–5958. https://doi.org/10.1021/cr068437y.